Effect of clocking on entropy noise generation within an aeronautical high pressure turbine stage

Lorenzo Pinelli[1a], Michele Marconcini[a], Roberto Pacciani[a], Friedrich Bake[b], Karsten Knobloch[b], Paolo Gaetani[c], Giacomo Persico[c]

[a] *Department of Industrial Engineering, University of Florence, Via S.Marta 3, 50139 Firenze, Italy*

[b] *Institute of Propulsion Technology, Dept. Engine Acoustics, German Aerospace Center (DLR), D-10623 Berlin, Germany*

[c] *Energy Department, Politecnico di Milano, Via Lambruschini 4, 20158 Milano, Italy*

Abstract

The article reports on a detailed experimental and numerical study of the clocking effect between entropy wave spot and stator leading edge on the entropy wave evolution and the indirect noise generation within a high pressure turbine stage. Experimental campaigns considering burner-representative temperature fluctuations injected upstream of an uncooled high-pressure gas turbine stage have been performed in the high-speed closed-loop test rig of the Fluid Machine Laboratory (LFM) of the Politecnico di Milano (Italy). Acoustic measurements focused on entropy noise generation have been carried out by the German Aerospace Center, DLR (Germany) with two flush mounted in-duct microphone arrays. URANS CFD simulations with and without entropy fluctuations imposed at the stage inlet were performed with the TRAF code, developed by the Università degli Studi di Firenze (Italy). A numerical post-processing procedure, based on the time and space discrete Fourier transform (DFT) of the conservative variables, has been implemented to extract the low-frequency content connected to the entropy fluctuations and indirect noise emissions. Simulations show an overall good agreement with the experiments, especially at the stage outlet thus confirming the possibility to predict entropy noise by means of URANS simulations with time

[1]Corresponding author: lorenzo.pinelli@unifi.it

varying inlet conditions. By exploiting the combination of experiments and simulations, the evolution of the entropy wave, the identification of entropy noise generation areas, and the evaluation of indirect noise emissions, for the different clocking positions were properly assessed. This study also demonstrates that this type of simulations can be used for the geometric design optimization of combustor/turbine coupling performing detailed parametric studies concerning the clocking position of the perturbation source in order to reduce the turbine-combustor interactions and the indirect noise emissions.

Keywords: entropy noise, indirect combustion noise, aeroengine noise, high pressure turbine, measurement techniques, URANS simulations.

---

1. Introduction

The Flightpath 2050 document describes the Europe's vision for the next generation aviation and sets out challenging objectives in order to protect the environment. Aviation has a crucial role to play in reducing noise as well as greenhouse gas emissions, regardless of the continuous traffic growth. One of the main document goals is the reduction of 65% in perceived noise emission relative to the capabilities of typical aircraft in 2000, so the noise reduction research is central to deliver the Flightpath 2050 vision.

Acoustic pollution from aircraft is basically due to airframe and engine noise. The first noise source is related to turbulent flows over lifting surfaces (wings) of not aerodynamically-shaped components as landing gears. Anyway the principal noise emissions come from engines where each component (fan, compressor, combustor, turbine, etc...) contributes to the overall noise signature.

At the dawn of civil aviation, the principal acoustic emission was the jet noise, which has been drastically reduced by the introduction of high-bypass ratio turbofan engines [1]. Once the jet noise emissions were abated, the other sources (previously masked by jet pressure fluctuations in the overall emissions) became more and more relevant. After the reduction of jet noise, fan and low pressure turbine emissions emerge in the aft and rear part of the engine and low noise design criteria together with the use of passive absorbers (liners) were introduced to reduce their impact on the engine noise signature. In this context, the combustion noise is now becoming relevant and deserve to be accurately studied in terms of emitted noise and related combustor instabilities.

Combustion noise can be split into two types depending on the acoustic generation mechanisms. The unsteady heat release connected to the fuel combustion generates local unsteady volume expansion that acts as acoustic "monopole" producing acoustic waves called direct noise. Indirect noise (or entropy noise) is generated when temperature or velocity fluctuations (caused again from the unsteady heat release) are accelerated when being convected downstream by the flow field. These fluctuations (called entropy and vorticity wave by the classical wave theory) are swept by the flow, and are silent if not accelerated. When entropy waves are accelerated (in a nozzle or in a stator channel), they acts as an acoustic "dipole" becoming a source of indirect noise [2, 3].

Early theoretical studies on entropy waves and their acoustic effects were conducted by Morfey [4], Marble and Candel [5], and Cumpsty and Marble [6] in the 1970s. Since then, analytical and experimental studies on this topic have been performed [7, 8]. More recently, a second golden age for the aeroacoustics (as firstly foresaw by Sir James Lighthill in 1992) has started increasing the number of numerical and experimental activities on this topic [9]. From the numerical point of view, more and more accurate schemes were created and implemented, and the increase of available computational power has lead to more complex unsteady simulations based on both URANS and LES methods. On the other hand, the experimental activities are focused on realizing test rigs closer to actual working conditions and on implementing accurate acquisition systems, especially for the unsteady temperature probes still limited in terms of acquisition frequency.

Experimental and numerical studies can be found for nozzles or high pressure turbine stage. Bake et al. [10] experimentally investigate the entropy noise generation in a convergent-divergent nozzle with a maximum Mach number of 1.2, while Huet et al. [11] propose a 2D model extended to choked flows to derive transmitted and reflected acoustic waves through a nozzle. In the same context, Duran and Moreau [12] had already presented a work where a solution of the quasi-1D Euler equations was derived for subcritical and supercritical nozzle flows. For pressure turbine stages, an experimental assessment on the indirect noise generation (for the same turbine stage numerically studied in this paper) can be found in the work from Knobloch et al. [13] and describes the main outcomes of the European Project RECORD. Numerical simulations based on LES approach, for entropy noise prediction of turbine guide vane were performed by Hu et al. [14] and by Winkler et al. [15], while a realistic turbine stage was studied by Becerril et al. [16].

This work reports on the natural continuation of previous studies by the authors who already presented an in-depth experimental [17] [18] and numerical study of hot streak propagation [19] and entropy wave evolution [20] within an high pressure turbine stage installed in the test rig at the Politecnico di Milano. Starting from the findings coming from these previous works, this paper is focused of the indirect noise emission of the high pressure turbine stage caused by an incoming entropy wave in four different clocking positions. To do so, the simulation strategy and the available post-processing techniques have been extended during the presented study in order to numerically evaluate the indirect noise generation and propagation mechanisms. For a single clocking position (the only EW configuration tested during the RECORD project), the numerical indirect noise results are compared with acoustic measurements acquired at the stage outlet highlighting an excellent agreement and confirming the capability of URANS approaches to predict entropy noise generation in turbine stages.

The incoming entropy waves are representative of burner temperature fluctuations in terms of spot shape, fluctuation frequency and total temperature variation percentage. Such waves are characterized by a low frequency (one order of magnitude lower than the blade passing frequency, BPF), a 10% total temperature fluctuation (which can be considered engine-representative), and their interaction with the stage basically generates a first harmonic pressure response in time. A dedicated numerical post-processing allows the accurate tracking of the entropy spot within the stage, the identification of the indirect noise generation regions, and finally the evaluation of the outgoing acoustic waves in terms of the sound power level at the stage inlet and outlet.

Thanks to the combination of experiment outcomes and simulation results, a deeper insight into the entropy noise generation and propagation mechanisms has been achieved. This study also suggests an useful and viable numerical process to assess the indirect noise emissions upstream and downstream the stage where indirect noise starts propagating through the machine and contributes to the overall acoustic emissions.

The paper firstly presents the experimental framework describing the turbine facility, the entropy wave generator and the thermal and acoustic acquisition systems. Then, the computational framework is reported focusing on the computational setup and the acoustic post-processing. Finally, the aerodynamic and indirect noise results are presented, compared with experimental acquisitions and discussed in details.

2. Experimental framework

The experimental side of this activity was carried out at the Laboratorio di Fluidodinamica delle Macchine (LFM) of the Politecnico di Milano (Italy). The entropy noise experiment involved a research turbine, an entropy wave generator (EWG) specifically designed for producing entropy waves, and microphone arrays to acquire and properly decompose the acoustic wave upstream and downstream the high pressure turbine stage.

The facility is described in detail in [17], the generation and character of the entropy waves is discussed in [18], and the acoustic acquisition system is presented in [13]. However, in this section, the main characteristics of the experiment are summarized to give a comprehensive view of the activity to the reader.

Parameters	**Stator**	**Rotor**
Blade Count	22	25
Aspect Ratio	0.83	0.91
Solidity	1.20	1.25
Angular speed [rpm]	-	7000
Outlet Mach number	0.59	0.45
Reynolds number	0.87×10^6	0.50×10^6
Stage Expansion Ratio	1.4	
Inlet Total Temperature T_R [K]	323.0	

Table 1: Operative and geometrical stage parameters.

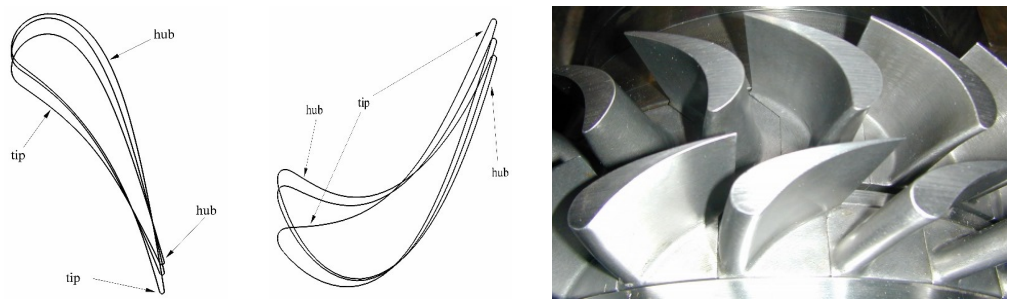

(a) (b)

Figure 1: HPT stage: (a) stator and rotor geometry, (b) stage picture.

2.1. HP turbine facility

The HP turbine stage is installed in a high-speed closed-loop test rig located at the Politecnico di Milano. The facility consists of a high-speed centrifugal compressor station and a cooler which supply flow rate and pressure ratio to the test section where the HPT stage is integrated. This research turbine is representative of a high pressure stage for aeronautical applications. For the present studies on entropy noise generation, the stage was operated in subsonic conditions, even though the rig is able to reach transonic operating conditions [17]. The most relevant geometrical and operative data are listed in Table 1.

Figure 1 reports on the left the rotor and stator profiles at different span sections, and on the right a picture of the stage: the relevant geometrical feature to be highlighted is the stator lean (12° on the pressure side, that influences the entropy wave transport in radial direction and thus the indirect noise generation within the stator vane [20]. For the present operating

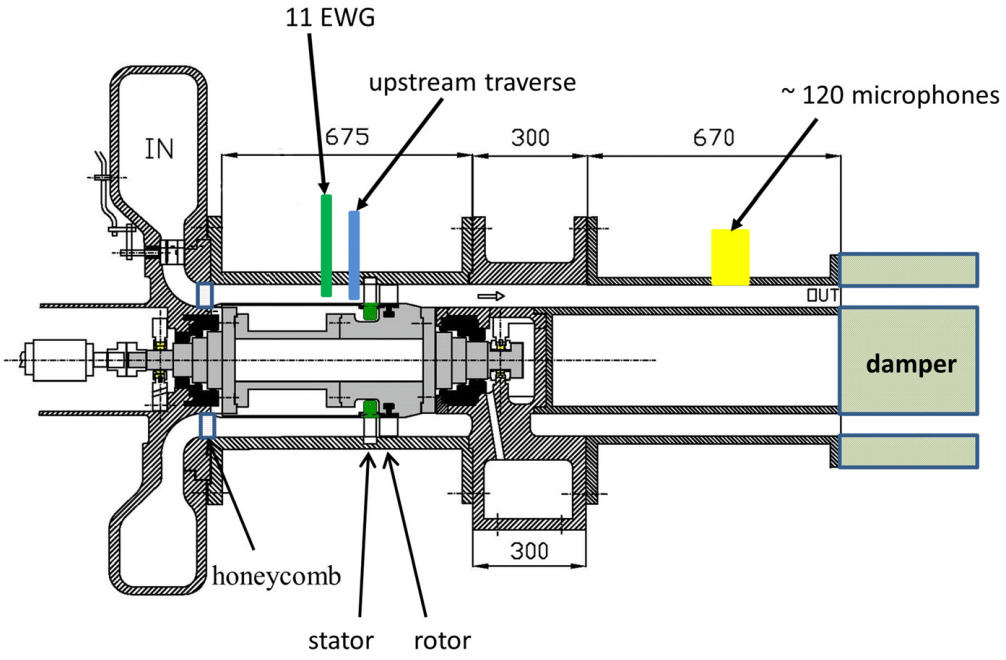

Figure 2: Test rig meridional view with entropy wave generator and acquisition systems.

condition, the flow remains subsonic both across the stator and the rotor (stator-exit Mach number at midspan ≈ 0.6, rotor exit relative Mach number ≈ 0.45) with Reynolds numbers (based on the blade chord and the discharge flow velocity at midspan) of 0.87×10^6 for the stator and 0.50×10^6 for the rotor (see again Table 1).

Figure 2 provides the meridional view of the test section where the turbine stage is installed. The stage is fed by a centripetal inlet guide vane (IGV) and the air goes through a straightener (honeycomb) and a straight annular duct before entering the stator vane. Inside the upstream duct the 11 entropy wave generators (EWG) are installed 2 stator axial chords upstream the stage. To guarantee a simple spatial periodicity and to allow the clocking studies, one injector out of two stator blades was installed (11 injectors that can be rotated around the machine axis, over 22 stator blade). The upstream traverse to acquire the entropy spots is placed between the EWG and the stator (one stator axial chord upstream from the stator leading edge).

At the stage outlet, a long straight section is installed, where the second microphone array is located around 15 rotor axial chords downstream the stage to measure the indirect noise generated across the stage. Downstream the microphone array an anechoic termination is also present (damper).

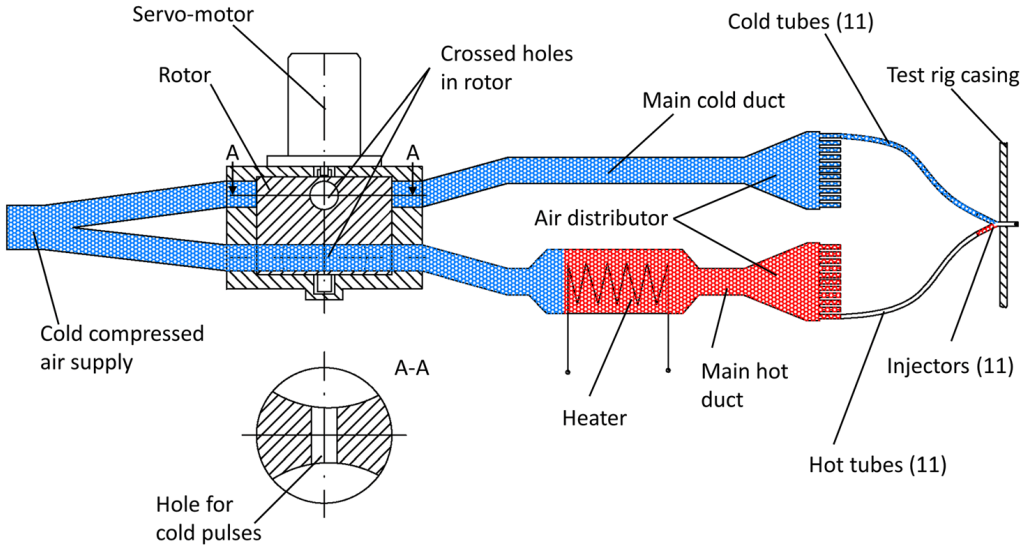

Figure 3: Entropy wave generator (EWG).

2.2. Entropy wave generator

The entropy wave generator (EWG) was specifically designed for this experimental campaign. Basically, the system reproduces the entropy spots released by burners by injecting hot and cold air alternatively at a defined frequency. The fluid coming from the injector is nearly in mechanical equilibrium with the main stream, thus minimizing the pressure perturbations connected to the pulsating injection. Experimental characterization of a single injectors [18] showed that the system generates a nearly-sinusoidal entropy wave (EW) spots whose shape are circular with a maximum temperature fluctuations up to 10% of the mean temperature level in order to produce engine-representative perturbations. The maximum achievable frequency is 100 Hz, and for the present research, the tests at 90 Hz were selected.

The EWG operation is outlined in Figure 3: compressed air is first split into two alternated branches by a rotating valve and one of the streams is heated by an electrical heater. Two conical diffusers distribute each stream into 11 tubes which are reconnected, in pairs, before each injectors exhaust. Preliminary experiments in a simplified nozzle environment [18] showed that, despite the stepwise form of the theoretical signal, the resulting entropy wave is significantly smoothed by the mixing process and the thermal dispersion take place in the tubes and the injectors, resulting in a sinusoidal entropy signal injected in the main flow.

The amplitude of entropy wave fluctuation depends on the flow conditions at the turbine inlet, on the thermal power provided by the heater, on the

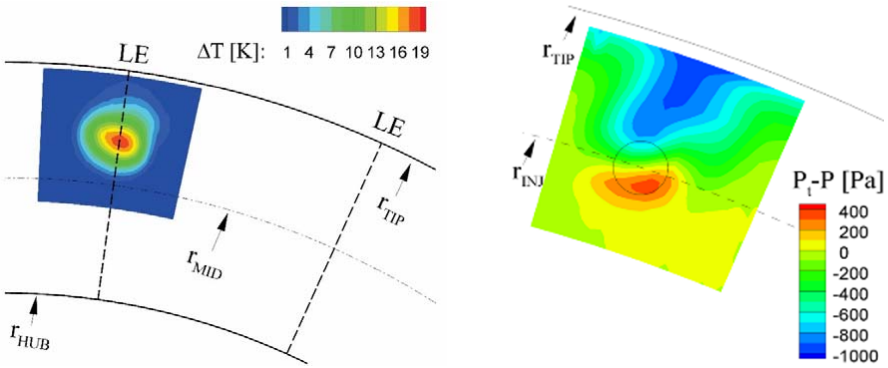

(a) (b)

Figure 4: Entropy spot measuremants at plane T0: (a) temperature fluctuation, (b) pressure fluctuation.

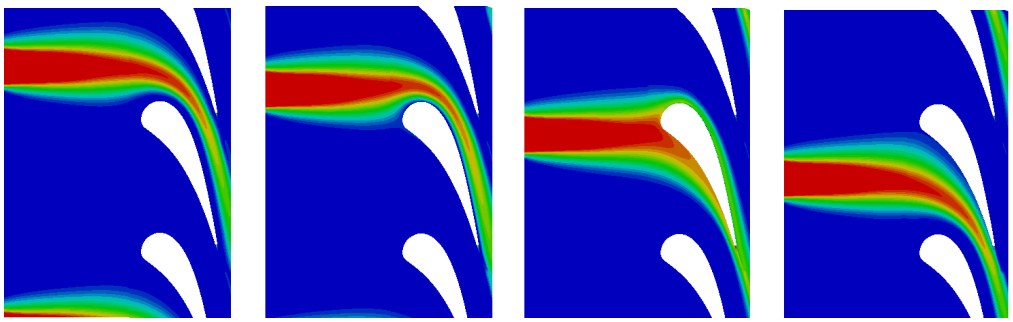

Figure 5: Definition of the entropy spot clocking positions (from numerical simulations): (a) MP case, (b) SS case, (c) LE case, (d) PS case.

feeding air pressure, and on the angular speed of the rotary valve. In the present case the trace of the entropy spot experimentally acquired at the plane T0 by the traversing system is depicted in Fig. 4.

Concerning the spot positions, the EW injectors were installed two axial stator chords upstream of the stage and were partially immersed into the flow, so that EW spots are released at 70% of the channel height. Four azimuthal positions were considered for injection, so to simulate four burner-stator blade clocking positions (see Fig. 5) and investigate clocking effect in the entropy noise generation. These positions were chosen to have EWs injected directly on the vane leading edge (LE case), at midpitch between adjacent blades (MP case), and in two further intermediate positions closer to the suction side (SS case) or the pressure side (PS case) of the stator. During the experimental campaign, it was observed that the mechanical equilibrium between the jet and the main stream produces slightly different velocities among the two streams: this fact, summed up to the injector wake and wall thickness, triggers high turbulence regions on the contours of the entropy waves. In turn, turbulence will promote the EWs diffusion on the surrounding flow as they are transported downstream.

2.3. Measurement techniques

The proper identification of the indirect noise emission and the study of entropy wave evolution within the stage require a combination of different measurement techniques. A brief description of the main measurement devices are reported in the following.

2.3.1. Acoustic measurements

For the acquisition of the outgoing pressure waves, microphone arrays were installed downstream the stage. The array consists of a four rings with 35-35-25-25 microphone layout equally-spaced with an axial distance of 22 mm among them. The microphones are G.R.A.S. 40 BP coupled to pre-amplifiers 26 A with a maximum allowable SPL of this combination of 174 dB. All microphones were calibrated prior to installation using the data acquisition described below and a piston-phone B&K4228 at 124 dB, 251Hz.

For the acquisition of the microphone signals and associated rig test data, a dedicated high-channel data acquisition system was used. It was a custom-built device from DLR ("Pandora 2") capable of recording up to 256 channels at up to 48 kHz and had a resolution of 24 bit. A shaft trigger signal (1/rev) and the trigger signal of the EWG device (pressure signal, amplified by factor 10) were acquired simultaneously with the microphone signals.

Concerning the acoustic mode analysis of the pressure fluctuation, a homogeneous flow without swirl is assumed. The Mach number values were derived from aerodynamic measurements. Further detail on the acoustic acquisition system and acoustic decomposition can be found in [13].

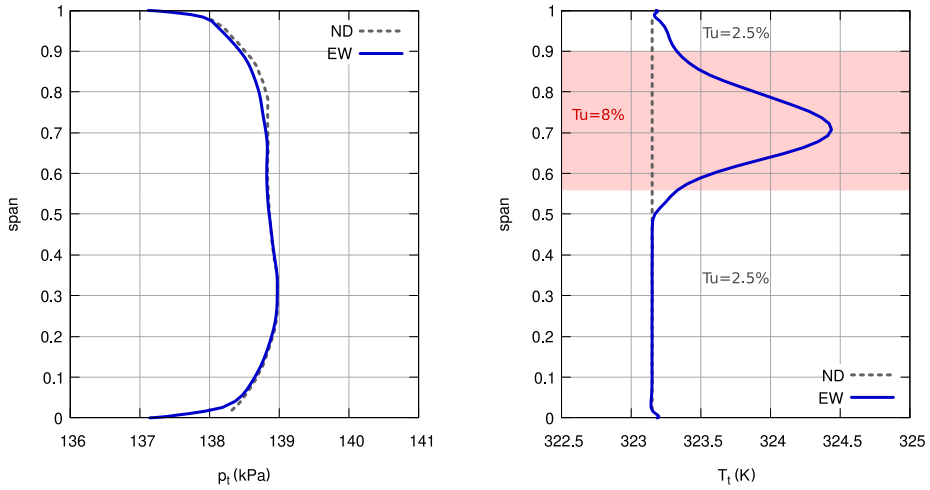

(a) (b)

Figure 6: Circumferentially averaged inlet profiles at the plane T0 for the clean case (ND) and the experiment with entropy wave (EW): (a) total pressure, (b) total temperature with turbulence intensity.

2.3.2. Aero-thermal measurements

Several measurement techniques were applied in the framework of the present experimental campaign as reported in Table 2. Both the aerodynamic and thermal fields were measured upstream and downstream of the stage, as well as in-between the blade rows. With reference to Fig. 2, the stage inlet traverse T0 is placed one stator axial chord upstream of the stator; traverse T1, in-between the blade rows, is placed 32% of the stator axial chord downstream of the stator; the stage-exit traverse T2 is placed 32% of the rotor axial chord downstream of the rotor.

The inlet total pressure profile at the stage inlet traverse T0 was measured by means of a flattened Pitot tube, while turbulence measurements were also performed with a single hot wire probe. Measurements indicated a flat total pressure profile (see Fig.6(a)) and a turbulence intensity of 2.5% far from the temperature spot. The turbulence intensity increases up to 8% between 55% and 90% of the span (see Fig.6(b)) where the EW spot is imposed, making the inlet condition more representative of real combustor burner fluctuations.

	Flow quantities	**Instrument**	**Uncert.**	**Prompt.**
T0	Main stream total pressure	Pitot tube	±60 Pa	steady
	Main stream turbulence	Hot wire	-	40 kHz
	Hot streak temperature	Thermocouple	±0.3 K	steady
	Entropy wave temperature	μ-thermocouple	±0.3 K	200 Hz
T1	Main stream quantities	Five hole probe	α =0.20°	steady
	Hot streak temperature	Thermocouple	±0.3 K	steady
	Entropy wave temperature	μ-thermocouple	±0.3 K	200 Hz
T2	Main stream quantities	FRAPP	α =0.25°	80 kHz
	Hot streak temperature	Thermocouple	±0.3 K	steady
	Entropy wave temperature	μ-thermocouple	±0.3 K	200 Hz

Table 2: Experimental measurements and techniques applied.

Three-dimensional steady flow measurements were performed on T1 with a miniaturized five-hole probe (5HP) featuring a probe head dimension of 1.4 mm. Unsteady flow measurements on the stage exit traverse T2 were carried out with a cylindrical single-sensor Fast Response Aerodynamic Pressure Probe (FRAPP). By combining acquisitions for multiple rotations around its own axis, the FRAPP is operated as a virtual three-hole probe and provide information on the time-periodic component of the total and static pressure

and blade-to-blade flow angle. Full details on the FRAPP technique and its most recent developments can be found in details in [21].

Time-resolved temperature measurement were performed on all the sections (T0, T1, T2) by means of a Fast micro-ThermoCouple (FTC): probe design and metrological characteristics are reported extensively in [18]. The important feature to be recalled is the FTC promptness that allows for a frequency response of 200 Hz (after digital compensation with the experimental transfer function, determined in shock tube tests).

The FTC has been always applied in the absolute frame of reference: this is clearly consistent with the physics downstream of the stator. When applied downstream of the rotor, the FTC frequency response is not enough for capturing the rotor evolution flow field (at 2.9 kHz): for this reason the FTC allows only to measure the EW features, thus making and average on the rotor flow property.

3. Computational framework

All the numerical simulations were carried out using the CFD TRAF solver [22] developed at the University of Florence. The TRAF code solves the unsteady, three-dimensional, Reynolds-averaged Navier-Stokes equations with a finite volume formulation on H-type and O-type structured grids. The discretization of convective fluxes is handled by a 2^{nd} order TVD-MUSCL strategy build on the Roe's upwind scheme [23], while a central difference scheme is used for the viscous fluxes. The turbulence closure is based on different turbulence model and for these analyses the Wilcox $k-\omega$ model [24] in its high-Reynolds formulation was selected. Unsteady simulations are performed by means of a dual-time stepping technique [25] with sliding interfaces between adjacent rows where linear interpolations are used to exchange the flow variable values. The conservative behavior of the interpolation method has already been proved by checking that acoustic waves are not altered across the interface.

A time-varying 2D inlet conditions can be used to impose the incoming fluctuations at a desired clocking position in terms of instantaneous values of flow angles, total temperature, total pressure and turbulence quantities (k and ω). The incoming disturbance is defined by means of a set of equally-spaced instants, which are linearly interpolated in time during the unsteady computation. The unsteady analyses can be performed with a full annulus

or phase lagged approach, and the time discretization depends on the highest frequency to be captured.

The high level of the code parallelization, achieved by means of a hybrid openMP/MPI code architecture [26] was exploited to reduce the computational time. The computational framework was extensively validated against several turbine and compressor configurations for aerodynamic, aeromechanical and aeroacoustic applications [27, 28, 29].

3.1. Computational setup

The numerical study consists of 5 unsteady runs: the first one is the clean case without the EW (NO-disturbance, ND) and further 4 cases with the incoming EW perturbation in the different clocking positions respect to the stator leading edge (PS, SS, LE and MP).

Since the rotor and stator blade numbers are prime each-other the unsteady simulations require the analysis of the entire stage wheel (including the 11 entropy spots, 22 stators and 25 rotors) in order to avoid any blade count modification that can alter the aerodynamic solution. A reduced an-

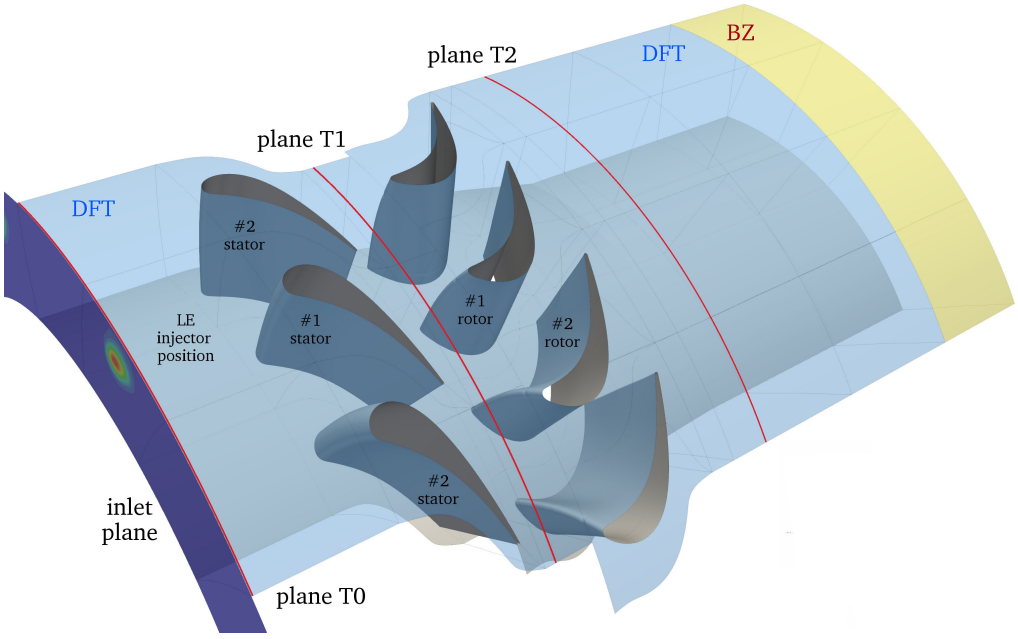

Figure 7: Computational setup.

gular sector describing around 1/7 of the computational domain is reported in Fig. 7.

The inlet boundary is placed at plane T0, where the EW spots are acquired by means of the upstream traverse system in the experimental campaign. On this boundary, 2D time-varying inlet conditions were used to impose the entering entropy wave. They impose local instantaneous values of flow angles and total temperature and pressure and also require the knowledge of the inlet free-stream turbulence to apply the boundary conditions for the turbulence model quantities. For this study, the free-stream turbulence intensity imposed at the inlet was locally increased from 2.5% (coming from measurement at the mid-span) up to 8.0% in the EW spot region (shown in Fig. 7) to include the effect of the presence of the injector device. An incoming turbulence intensity of 2.5% means a transitional regime in terms of boundary layer state, nevertheless due to the high local values in the EW spot (8.0%) it has been decided to use the high-Re fully turbulent Wilcox model. With this turbulence model, the y^+ value for the first grid point above the wall surface is kept below 2. The use of a coupled turbulence transition model would have been more appropriate for the blade surfaces far from the EW impingement effect (hub and mid-span), yet it would have required a lower value of y^+ thus increasing the already expensive computational requirements. All the inlet conditions are applied by means of a non reflecting characteristic-based method [30] thus ensuring that no additional sound is introduced.

Looking again at Fig. 7, the outlet plane is located around 3 rotor chords downstream to the plane T2. A buffer zone (BZ) was included at the domain outlet to avoid pressure wave spurious reflections which could pollute the overall solution by interacting with the inner domain. The buffer zone was created as a stretched grid area where higher numerical dissipation (four times the standard value) is applied during the simulations. The buffer zone axial extension and stretching are defined taking into account the wavelength of the main acoustic fluctuations coming from rotor/stator interactions and from the pulsating inlet leading to cells 10 times bigger than the inner elements. Such domain area ensures that the domain outlet becomes non-reflective by dissipating the fluctuation coming from the interior domain before reaching the exit section where a fixed back-pressure is imposed. The correct working of this NRBC (non-reflecting boundary condition) was verified by decomposing the pressure field before the BZ inlet in the inner domain and looking at the upstream pressure waves.

Finally, no slip and adiabatic conditions are applied to all the wall surfaces.

Stator and rotor passages are discretized by using structured elliptic O-type grids with a mesh density which ensures at least 30/40 cells for the shorter wavelength among the acoustic, vorticity and entropy waves, which can be computed before the unsteady runs once the mean aerodynamic quantity are known by means of a prior steady state simulation. Following this rule, stator mesh is defined by 424×64×88 cell along the blade, in pitchwise, and spanwise directions respectively, while the rotor grid has $448 \times 64 \times 88$ cells. Near the blade and endwall surfaces the grid is reclustered to accurately solve the boundary layers. H-type blocks with similar grid density are placed at the stage inlet and outlet and in the inter-row area.

The time discretization was selected to solve the main Blade Passing Frequencies (BPFs) and so a complete wheel resolution was computed by using 625 time steps (at each time step the rotor rotates of 360°/625). Previous studies by the authors reported a sensitivity study on the effect of the temporal discretization in the TRAF results [31].

In order to decrease the overall computational time, the entropy wave frequency (EWF) was slightly modified from 90 Hz to 116.6 Hz, which corresponds to the rotor rotational frequency. This frequency modification sets the simulation period to the stage rotational one (8.5 ms), so that a single EW pulsation occurs during one rotor revolution. The accuracy of this approach was confirmed by an additional computation (for a single injector position) with a 5 times larger period (42.8 ms) where 4 EW pulsations at 92.8 Hz take place during 5 rotor revolutions with the same time discretization. The latter computations showed a practically identical EW evolution and indirect noise generation when compared to the 116.6 Hz EWF analysis. For this reason all the clocking simulations have been carried out with a EWF = 116.6 Hz reducing the CPU time by a factor of 5. Such a low frequency is fully resolved by the simulation as it is 25 times lower than the higher BPF (2916.6 Hz).

Each unsteady simulation has been run for 4 rotor revolutions (34 ms) and the solution periodicity was verified by looking at the blade lift fluctuations, the mean performance quantities and acoustic emission. These quantities must have the same time history between successive revolutions to confirm the convergence to a periodic solution. Each period, discretized with 625 time steps, means a time sampling $\Delta t = 0.014$ ms, ensuring a CFL (Courant–Friedrichs–Lewy) number ≈ 0.8. During the fourth period, which always fulfilled the convergence criteria, a run-time DFT algorithm was ac-

tivated in order to extract the Fourier coefficients in time of the conservative variable fluctuations at the harmonic of interests for the study of the EW evolution and the entropy wave noise emissions. With the above mentioned Δt, the maximum frequency resolution is around 36 kHz well above to the frequencies under investigation. About 24 CPU hours were needed for each time period on a Linux cluster of Intel CPU E5-2680 at 2.8 GHz using 150 processors.

3.2. Unsteady post-processing and acoustic wave extraction

The numerical solutions include two main sources of unsteadiness: the first one coming from the EW fluctuation entering the stage (low frequency content) and the second one driven by the stator/rotor interaction (high frequency content). In order to separate the low frequency content due to the EW fluctuations from the overall unsteady solution, a dedicated post-processing, based on Fourier coefficients has been implemented in the CFD framework. The method is based on the acoustic post-processing concepts described by Giles [30] and allows the filtering of total temperature fluctuation and the noise emissions at a given frequency, thus reproducing the experimental acquisition performed by the μ-thermocouple (with a frequency response of 200 Hz) and by the microphone arrays.

The numerical post-processing procedure starts with the time DFT of the instantaneous conservative flow variables $\mathbf{U}$ activated during the last period of each unsteady simulation in order to obtain the Fourier coefficients at the selected engine orders (EOs). The complex DFT coefficients can be handled as phasors quantities $\mathbf{U}_\delta^{\mathrm{EO}}$ that describe the small-amplitude sinusoidal oscillation of the conservative variables at the EO frequency.

$$\mathbf{U}_\delta^{\mathrm{EO}} = \begin{pmatrix} \varrho_\delta \\ (\varrho c_x)_\delta \\ (\varrho c_y)_\delta \\ (\varrho c_z)_\delta \\ (\varrho u_t)_\delta \end{pmatrix} \tag{1}$$

where the subscript δ denotes the small-amplitude phasor quantities, ϱ the density, $c_{x,y,z}$ the velocity components and u_t the total specific energy.

The DFT algorithm in time is directly implemented in the TRAF code and can be activated for selected domain blocks to extract only the time harmonics of interest (EO) achieving a substantial saving of memory and

storage requirement since it is not necessary to save the complete unsteady solution over a period for the successive post-processing by means of the DFT decomposition.

Using the first order approximation and neglecting the high order terms, the velocity phasors can be obtained from conservative variable phasors as follow:

$$\begin{aligned} c_{x\delta} &= \left((\varrho c_x)_\delta - \overline{c}_x \varrho_\delta\right) / \overline{\varrho} \\ c_{y\delta} &= \left((\varrho c_y)_\delta - \overline{c}_y \varrho_\delta\right) / \overline{\varrho} \\ c_{z\delta} &= \left((\varrho c_z)_\delta - \overline{c}_z \varrho_\delta\right) / \overline{\varrho} \end{aligned} \tag{2}$$

where quantities with overline refer to mean values. To complete the switch from conservative to primitive variables the overall pressure phasor can be computed as:

$$p_\delta = (\gamma - 1)\left(\frac{1}{2}\overline{c}^2 \varrho_\delta - \overline{c}_x(\varrho c_x)_\delta - \overline{c}_y(\varrho c_y)_\delta - \overline{c}_z(\varrho c_z)_\delta + (\varrho u_t)_\delta\right) \tag{3}$$

Finally, the local splitting technique based on characteristic waves method described by Giles in [30] is applied to separate upstream and downstream running pressure perturbations p_δ^- and p_δ^+ from the overall pressure phasors. The characteristic decomposition is based on the following assumptions: the viscosity can be neglected, and the flow variables can be locally linearized and considered 1D in the post-processing planes. First of all, the two characteristics $C^\pm$ related to acoustic waves are computed as follows:

$$C^\pm = \pm\,\overline{\varrho}\, c_s\, c_{x\delta} + p_\delta \tag{4}$$

where c_s is the sound speed. Then, the flow field perturbation quantities related to upstream and downstream acoustic waves become:

$$\begin{aligned} \varrho_\delta^\pm &= C^\pm / (2\, c_s^2) \\ v_{x\delta}^\pm &= C^\pm / (2\, \overline{\varrho} c_s) \\ p_\delta^\pm &= C^\pm / 2 \end{aligned} \tag{5}$$

Only the $c_{x\delta}$ component is reported as the only velocity component needed to compute the acoustic intensity in an annular section normal to the stage axis aligned along x direction.

By virtue of this numerical technique the stage outgoing acoustic waves can be evaluated in terms of SPL or PWL. The local SPL value can be

straightforwardly obtained from p_δ^- and p_δ^+, while it is necessary to compute the acoustic intensity vector to obtain the sound power and in turn the PWL. The sound power W_a is thus computed by integrating the acoustic intensity $\mathbf{I_a}$ over a section Σ of the annular duct and by taking the time average of this integral quantity.

$$W_a \;=\; \int_\Sigma \mathbf{I_a} \cdot \mathbf{n}\, \mathrm{d}\Sigma \tag{6}$$

where $\mathbf{n}$ is the surface normal unit vector. Within an annular duct, the acoustic intensity can be written as the following expression provided by Myers [32]:

$$\mathbf{I_a} = \left(\frac{p_\delta}{\varrho} + \mathbf{c}\cdot\mathbf{c}_\delta\right)(\varrho\mathbf{c}_\delta + \varrho_\delta\mathbf{c}) + \varrho\mathbf{c}T_{s\delta}s_\delta \tag{7}$$

which is valid for an arbitrary steady background flow in absence of body forces and neglecting the thermo-viscous terms and where p is the pressure, c the velocity vector, T_s the static temperature and s the entropy.

Moreover, when studying the entropy noise, it is also essential to extract the entropy wave evolution by computing the total temperature fluctuations. To do so, complex coefficients of the density and pressure are inserted in the perfect gas law (in the phasor formulation) to firstly obtain the static temperature phasor as follow:

$$T_{s\,\delta} \;=\; \left(\frac{p_\delta}{R} \;-\; \overline{T}_s\, \varrho_\delta\right) / \,\overline{\varrho} \tag{8}$$

where R is the gas constant.

The accuracy and robustness of the presented wave separation strategy was verified by using a radial mode analysis (RMA) decomposition, already used by the authors in [29], that produced very similar results. Although the used method is based on 1D assumption, the authors preferred to use the Giles theory instead of RMA because such a strategy considers the 2D distribution of the main flow field not needing for a circumferential average as for RMA analysis. Moreover RMA requires the prior computation of the acoustic mode-shapes by solving an eigenvalue problem that may result particularly stiff for very low frequencies.

Finally, by using the total temperature formula for the fluctuation, the complex coefficient of the total temperature can be derived as:

$$T_{t\delta} \;=\; T_{s\,\delta} \;+\; \frac{\gamma \;-\; 1}{R\,\gamma}\left(\overline{c}_x\, c_{x\delta} \;+\; \overline{c}_y\, c_{y\delta} \;+\; \overline{c}_z\, c_{z\delta}\right) \tag{9}$$

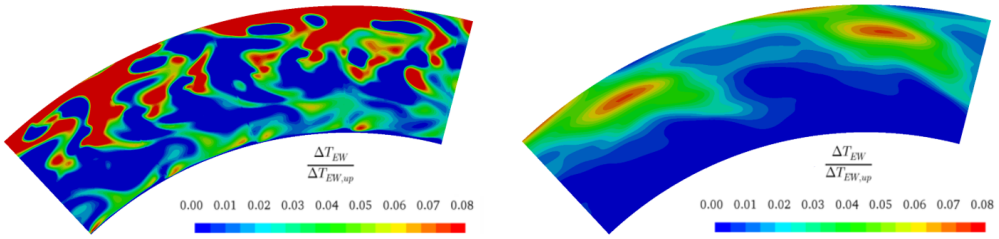

(a) (b)

Figure 8: Comparison of different approaches to extract the total temperature fluctuation (rotor exit, MP case): (a) instantaneous fluctuation (point-to-point difference with clean case), (b) filtered fluctuation by means of Fourier decomposition and phasor algebra. All the value are normalized with the maximum fluctuation at the inlet ($\Delta T_{EW.up}$= 19 K).

where γ is the heat capacity ratio. This phasor quantity, was proven to be extremely useful for tracking the entropy wave evolution within the stage [20, 33]. According to the phasor definition, by taking the real part of the total temperature and the pressure rotating phasors it is possible to rebuild the sinusoidal time history of the EW spot evolution and of the acoustic spinning waves. On the other hand, the phasor magnitude of the $T_{t\delta}$ defines the path of the spot as the envelope of the distortion evolution while being convected and interacting within the stage. $|T_{t\delta}|$ visualizations are used in the following for the comparison with the μ-thermocouple acquisitions on plane T1 an T2 and for the visualization of EW spot evolution, migration and interaction within the stage.

To follow the spot evolution, such visualizations are preferred with respect to instantaneous unsteady field point-to-point difference with ND clean case, as they focus only on the selected harmonic (that is the low frequency content of the EW), removing any other source of unsteadiness at higher frequencies present in the signal (see the comparison in Fig. 8).

4. Results and comparisons

Starting from the work on the entropy wave evolution [20], the numerical investigations were carried on and the unsteady post-processing was extended to extract the indirect noise emissions. This section collects all the results related to the indirect noise generation and propagation for the different clocking positions. Finally, the sound pressure level computed at the outlet

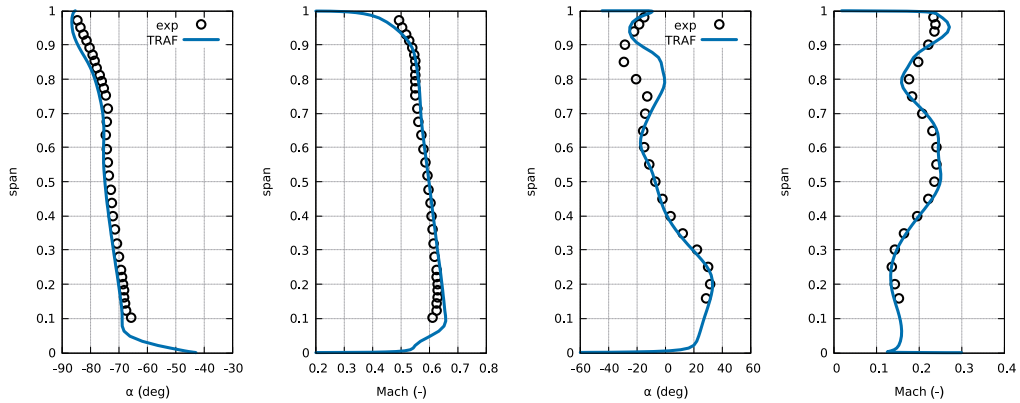

Figure 9: Spanwise distributions of blade-to-blade angle and Mach number (clean case): (a) stator exit (plane T1), (b) rotor exit (plane T2).

of the stage has been compared with experimental acquisition for the PS case showing a good agreement.

The first numerical and experimental comparisons concern the aerodynamic quantities for the clean case (ND). Spanwise profiles of time-averaged flow angle and Mach number are reported in Fig.9. At the stator exit (see Fig.9(a)), despite a small shift in the absolute flow angle distribution, due to a slight underestimate in the calculation with respect to the experimental data, the overall agreement can be considered very good. Looking at the rotor exit plane, the computed and measured spanwise distributions of absolute flow angle and Mach number are again in satisfactory agreement (see Fig.9(b)). Some discrepancies can be observed in the outer 30% of the span in the absolute flow angle distributions. Due to the quite low aspect ratio of the rotor blade, tip leakage effects dominate in this region and such differences are expected to be related to the tip clearance model adopted for the calculations. Such comparisons confirm the accuracy of the numerical setup from the aerodynamic point of view and are the basis for the following simulations with the incoming entropy waves.

Moving to EW simulations, and before showing the indirect noise results, it is also interesting to discuss the effect of the 11 EW spots on the blade loads for the different injector positions in comparison with the clean case (ND). The non-dimensional unsteady loads on two adjacent stators (defined in Fig. 7) are reported in Fig. 10(a) for the LE case. The loads come from

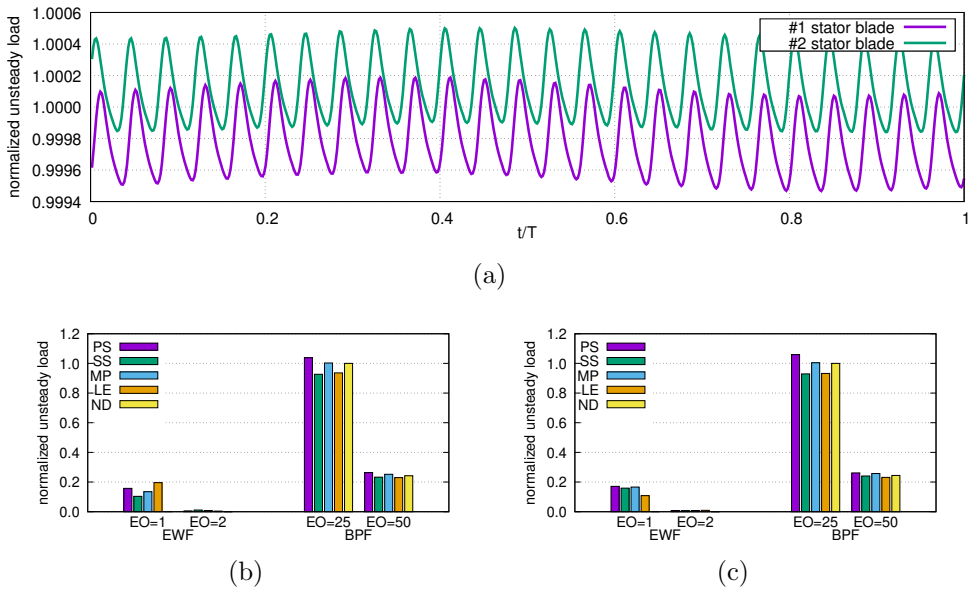

Figure 10: Numerical unsteady loads of 2 adjacent stator blades: (a) normalized time signal during a single rotor revolution (LE case), (b) frequency spectrum normalized with ND 1×BPF value (#1 stator), (c) frequency spectrum normalized with ND 1×BPF value (#2 stator).

the integration of the pressure field over the blade surface and are normalized with the mean value. As can be seen, the load time history is characterized by the 1×BPF of the rotor caused by its potential effect (25 peaks, at 2916.6 Hz, EO=25), yet a load modulation due to a single EW passage (at 116.6 Hz, EO=1) is clearly visible. The shift on the average lift value is due the injector wakes characterized by a non-uniform p_t and T_t mean field at the plane T0. The numerical unsteady load spectra of these two adjacent stator blades normalized with the clean case are reported in Figures 10(b) and 10(c). As expected, the rotor 1×BPF (EO = 25) is the highest source of unsteadiness and 2×BPF (EO = 50) is present. Focusing on the fluctuations caused by the EW, the first harmonic 1×EWF (EO = 1) is comparable to the 2×BPF (EO = 50), while the second harmonic 2×EWF (EO = 2) is negligible, as also confirmed by the experimental acquisitions. On the first stator blade, the LE position generates the maximum load oscillation, as this profile separates the entropy spot in two branches, while the lowest variation is connected to the SS case. On the other hand, the second stator profile experiences the lowest effect for the LE injection that mainly affects the first blade.

The same investigations were conducted on two adjacent rotors, defined in Fig. 7. Again, the principal contribution to flow unsteadiness is due to

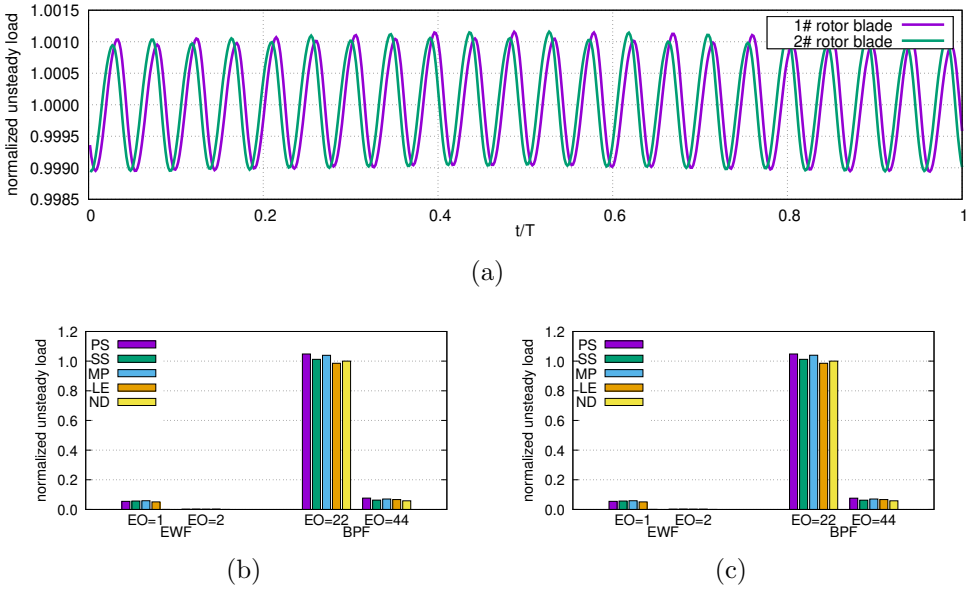

Figure 11: Numerical unsteady loads of 2 adjacent rotor blades: (a) Normalized time signal during a rotor revolution (LE case), (b) Frequency spectrum normalized with ND 1×BPF value (#1 rotor), (c) Frequency spectrum normalized with ND 1×BPF value (#2 rotor).

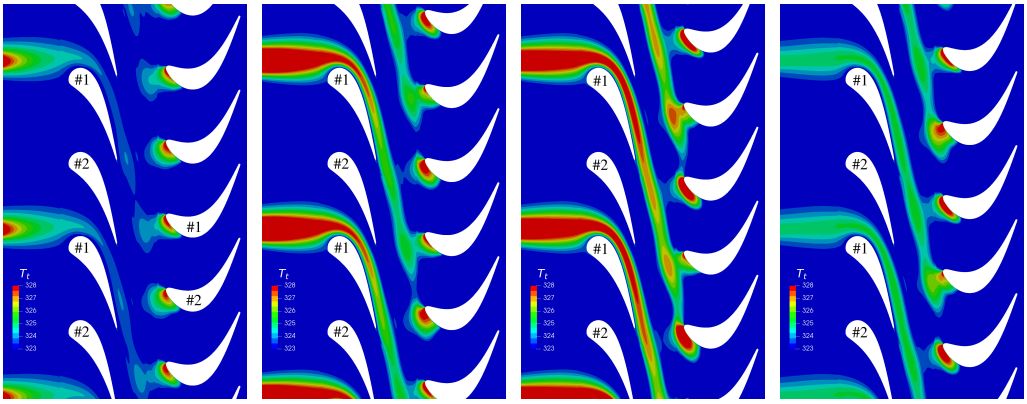

Figure 12: Time evolution of the EW spots (SS case): (a) $t/T = 0.00$, (b) $t/T = 0.25$, (c) $t/T = 0.50$, (d) $t/T = 0.75$.

the stator wake passage at the 1×BPF (EO = 22), that is the 22 peaks visible in Fig. 11(a)). Due to the rotation, the rotor blades undergo the same load history with just a time shift caused by their different tangential position. The load modulation due to the entropy wave is still visible, but is quite low when compared with the stator suggesting that the main generation of the entropy noise is located within the stator channel. Looking at the load spectra for the rotor rows the 1×EWF (EO = 1) is again comparable with the 2×BPF (EO = 44), and the 2×EWF (EO = 2) is practically zero. The four clocking positions have a similar effect on the first harmonic at the 1×EWF and the highest interactions are related for SS and MP positions where the EW spots result less diffused when propagating thorough the stator as shown in the following.

4.1. Entropy wave propagation

The entropy wave evolution within the stage (see Fig. 12) and its effect on rotor secondary flows has been described in a previous paper by the authors [20]. This section summarizes the main outcomes and adds additional numerical results that are necessary to understand the indirect noise generation process and propagation phenomena.

4.1.1. Stator row

The entropy wave footprint through the stator channel can be tracked by plotting the iso-contours of the $|T_{t\delta}|$. As already stated, this quantity is able to describe the spot envelope path and its attenuation while being convected by the mean flow. Figure 13 depicts the iso-contours of this quantity through the stator vane for the different clocking positions. It is clearly visible the complex interaction for the LE case where the entropy spot is cut into two branches convected downstream on the pressure and suction side. For the other positions, the spot remains quite compact with a circular shape and migrates in a different radial position depending on the clocking injection. Among the clocking positions, the SS case experiences the minimum diffusion of the temperature spot. All numerical simulations predict about 3-4 K reduction at the stator exit for all the cases in agreement with the experimental acquisitions.

The accuracy of the numerical predictions is confirmed when looking at the experimental acquisition of the temperature fluctuation in the inter-row region (plane T1). The numerical and experimental comparisons for all the

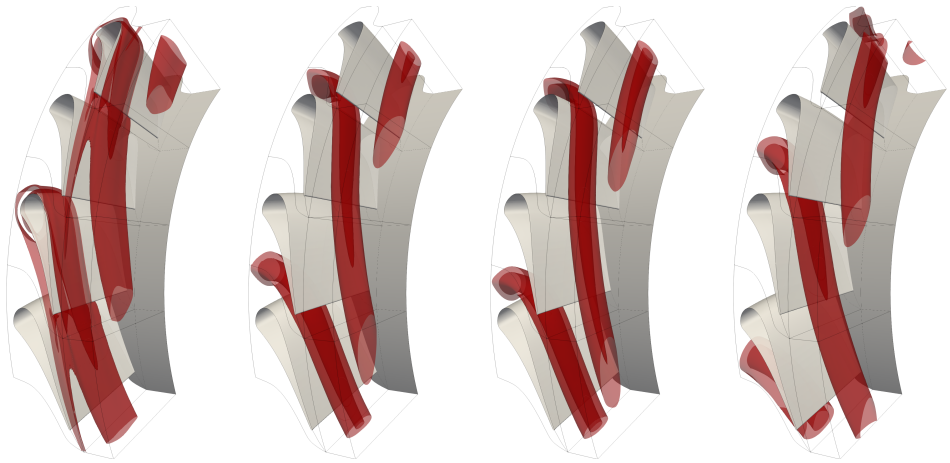

Figure 13: Spatial evolution of the EW spots through the stator from numerical simulations: (a) LE case, (b) MP case, (c) SS case, (d) PS case (iso-contours of $|T_{t\delta}|$: outer contour $|T_{t\delta}|$=1.0 K, inner contour $|T_{t\delta}|$=1.7 K).

clocking positions are collected in Figure 14 that reports the total temperature maximum fluctuations ($\Delta T_{\mathrm{EW}} = |T_{t\delta}|$) divided by the maximum total temperature difference of the incoming entropy spot ($\Delta T_{\mathrm{EW,up}} = 19$ K). In general, the numerical simulations show a lower spread of the hot spot due to the well-known lack of diffusion of URANS methods, yet the numerical results are globally in agreement with the experimental data. Moreover, these comparisons show that the spanwise migration of the spot is strongly dependent on the clocking position and thus with the interaction with the blade averaged pressure field.

In details, the spot, injected close to the pressure side, is pushed towards the hub; conversely, when injected close to the suction side, the entropy wave remains at higher span being pushed towards the tip and the T_t peak is more intense. These migrations are due to the opposite pressure gradients activated on the two blade sides by the 3D leaned design of the stator blade and are correctly captured by the simulations. MP case shows an evolution in the middle between PS and SS results, while a different interaction is found for the LE case where, as already shown, the EW spot is cut by the blade leading edge and covers the blade surface accumulating the high temperature spot within the boundary layer and bringing the entropy spot along the blade wake where the downwash of the low momentum fluid promote a further

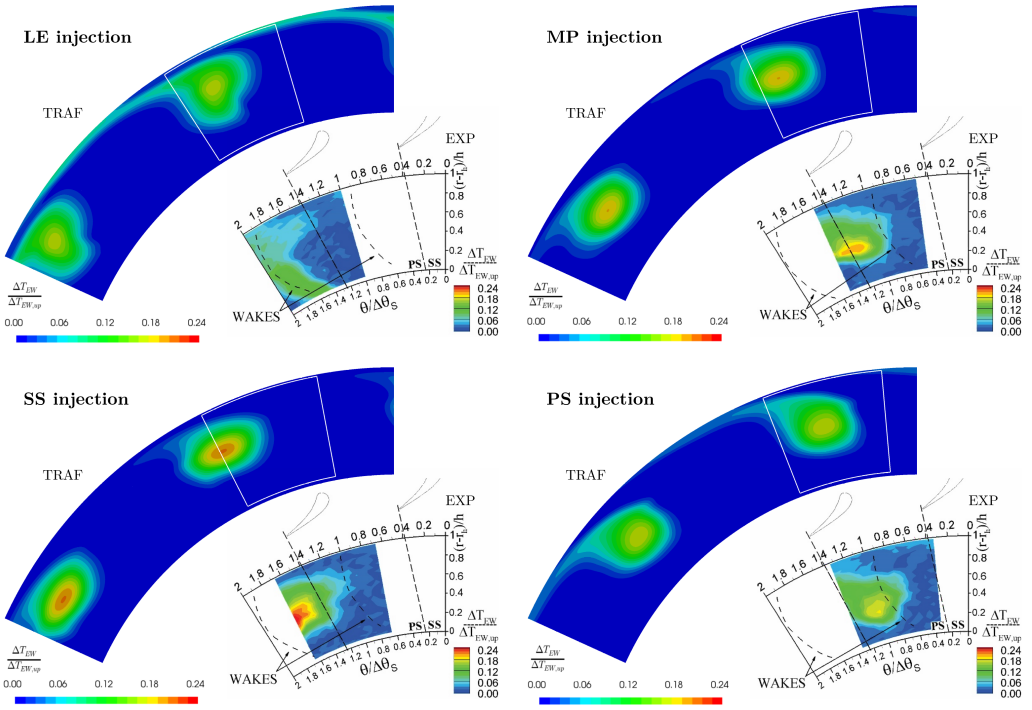

Figure 14: Amplitude of EW temperature oscillations at the stator-exit (T0) for the four different injector-stator clocking positions: comparison between numerical results (top sector) and experimental acquisitions (bottom sector).

migration of the spot towards the hub regions.

4.1.2. Rotor row

After the propagation within the stator vane, the entropy wave spot is convected thorough the rotor channel where the EW evolution is mainly driven by the unsteady interaction between the entropy spots and the rotating profiles. The maximum and the minimum diffusion of the entropy spot are for the PS and SS case respectively. Figure 15 depicts these two opposite cases: for the PS case the EW interacts with the rotor hub secondary flow (that extends up to midspan) and the hot fluid is spread for about half of the pitch in the hub region. On the other hand, for SS injection, the spot results more compact and migrates towards the tip region. This can be explained by considering that, due to the stator blade leaned shape, the entropy wave has entered the rotor above midspan and this has probably promoted the interaction with the rotor tip leakage and secondary flows.

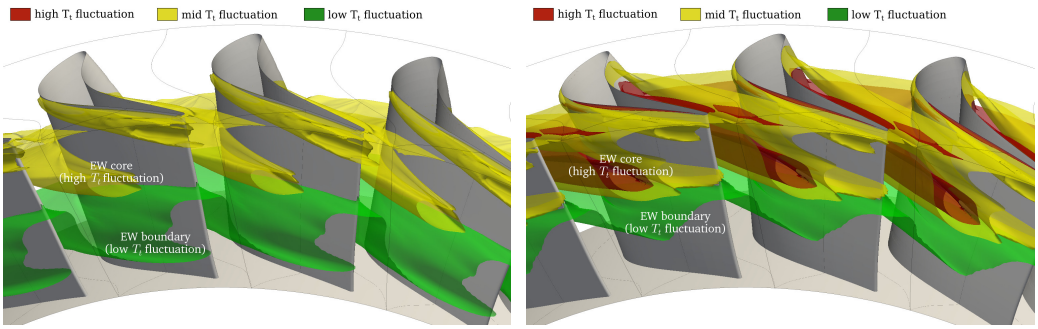

(a) (b)

Figure 15: EW path in the rotor: (a) for the maximum (PS case), and (b) for the minimum (SS case) diffusion of the EW spot from numerical simulations (iso-contours of $|T_{t\delta}|$: high T_t fluctuation contour at $|T_{t\delta}| = 1.2$ K, mid T_t fluctuation contour at $|T_{t\delta}| = 0.8$ K and low T_t fluctuation contour at $|T_{t\delta}| = 0.4$ K).

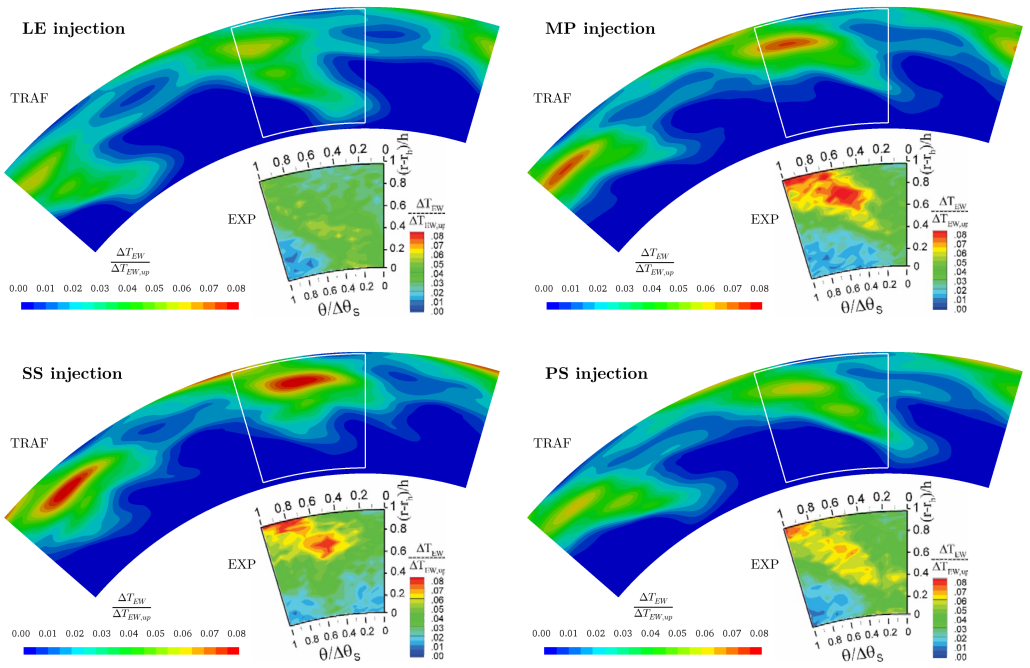

Figure 16: Amplitude of EW temperature oscillations at the rotor-exit for the four different injector-stator clocking positions: comparison between numerical results (top sector) and experimental acquisitions (bottom sector).

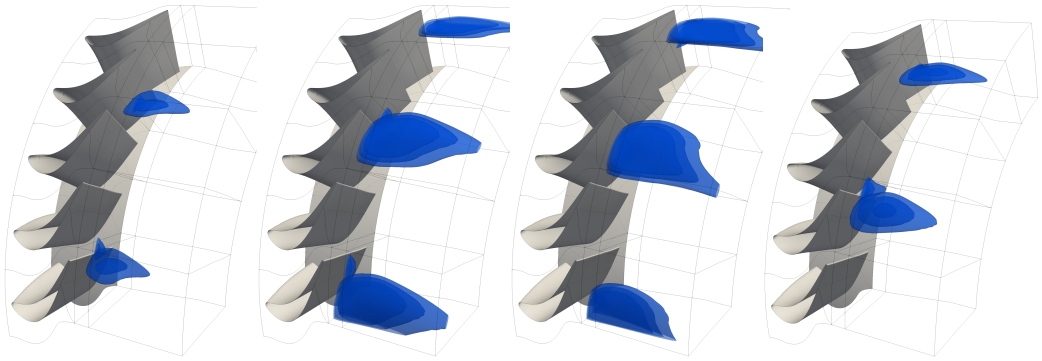

(a) (b) (c) (d)

Figure 17: Spatial evolution of the EW spots downstream the rotor from numerical simulations: (a) LE case, (b) MP case, (c) SS case, (d) PS case (iso-contours of $|T_{t\delta}|$: outer contour $|T_{t\delta}|$=0.5 K, inner contour $|T_{t\delta}|$=0.6 K).

As for the stator row, the comparison with the temperature fluctuations acquired during the experimental campaign is performed at the rotor exit (plane T2) in the inertial frame of reference in terms of $|T_{t\delta}|$ for the different clocking positions.

Such comparisons are collected in Figure 16 highlighting an excellent agreement and confirming the capability of the numerical procedure to correctly predict the entropy evolution of EW. Experimental and numerical outcomes reveal a temperature reduction less than 2 K across the rotor, and the presence of the additional temperature gradients due to the EW reduces the secondary flows as already described in [20] by the authors.

Finally, by exploiting the above mentioned fluctuation post-processing, the 3D shape of the EW envelope downstream the stage in the fixed reference can be extracted as iso-contour (see Fig. 17): it is evident the high distortion of the EW spot from the original circular shape.

Such information can result useful to design a successive stage by selecting a clocking position able to reduce the interaction with the convected entropy spot by avoiding the impingement of the hot spot with the leading edge of the successive stators.

4.2. Indirect noise generation

The presented post-processing was proven to correctly track the temperature distortion within the high pressure stage and suggest that the indirect

noise generation phenomena are correctly captured by URANS analysis. For this reason the post-processing strategy has been further extended to study the indirect noise generation and propagation. Pressure fluctuations are thus extracted at the EWF and spatially decomposed to separate circumferential patterns and upstream and downstream running components in order to compute sound power level (PWL) for each single acoustic wave.

4.2.1. Stator row

The acceleration of the entropy spot which transports a non acoustic density fluctuation, generates a fluctuating force which acts as an acoustic "dipole" and thus a source of the indirect noise [3]. A second source of sound is related to the to density fluctuations due to the entropy wave that lead to unsteady loads on the blades (as observed in Fig.10). This unsteady load generates an acoustic field by virtue of the third law of Newton as shown in [34] and [35] that interacts and modulates the sound created by entropy acceleration.

According to these physical explanations, the highest indirect noise sources are expected to be located within the stator channel where the higher velocity gradients occurs and depends on the EW clocking position. Figure 18 reports the numerical and experimental Mach number fields that clearly highlight the high velocity gradient zones.

Figure 19 pinpoints the zones where the indirect noise generation occurs:

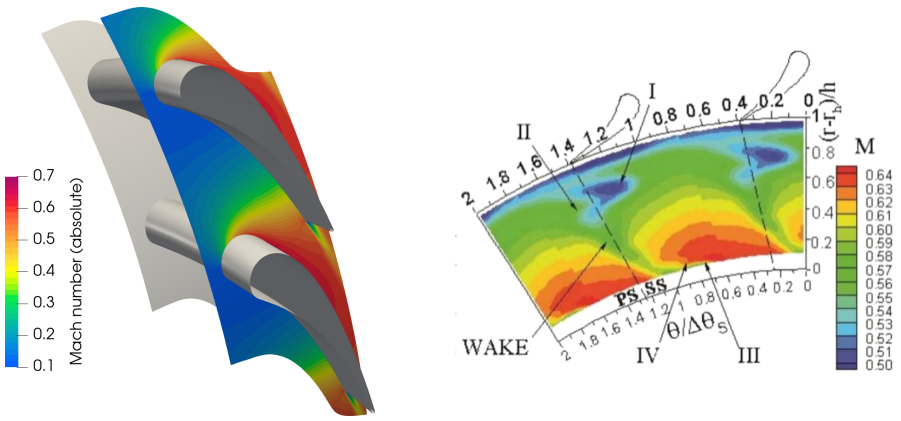

(a) (b)

Figure 18: Mach number field in the stator row to highlight high gradient areas. (a) Blade-to-blade numerical contours, TRAF. (b) T1 plane experimental contours.

the red solid surfaces depict the iso-contour of pressure fluctuation inside which the local SPL value is higher than 120 dB, while the blue transparent contours represent the EW envelope passing thought the stator. The four clocking positions reveal different morphology of pressure fluctuation, in detail:

- LE case: the main areas of indirect noise generation are located at the leading edge of the blade which cuts the entropy spot (upper blade). High level of pressure fluctuation is also found on the suction side of the lower blade due to the EW branch convected downstream near the pressure side of the upper profile. Moreover, the variations of density affecting the blade are stronger, and therefore the unsteady load is higher, explaining why LE case produces produces the largest amount of noise as shown in the following.
- MP case: the indirect noise sources are located only in the channel where the EW is convected downstream both on the first part of the

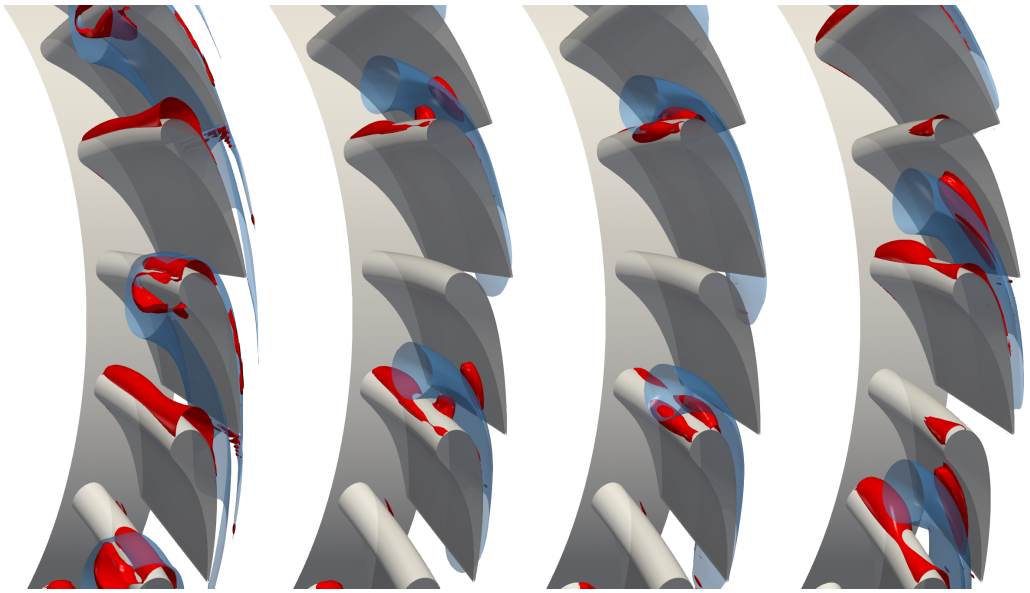

(a) (b) (c) (d)

Figure 19: Indirect noise generation areas for different clocking positions in the stator: (a) LE case, (b) MP case, (c) SS case, (d) PS case. Red solid surfaces delimit the zone where the pressure fluctuations are higher than 120 dB. Blue transparent contours depict the entropy wave path (numerical results).

suction surface and near the trailing edge on the pressure side around the 70% of the span.

- SS case: again the indirect noise generation zones are limited on the suction side faced on channel where the EW passes through. This position reveals the minimum generation effect within the stator channel.

- PS case: this case shows generation area similar to the MP case with an higher generation area on the pressure surface near the trailing edge.

Overall, the locations of the indirect noise generation zones are on the blade surfaces closest to the entropy wave spot where the maximum velocity gradient occurs (see Fig. 18). These areas are located on the suction side at the leading edge, and of the pressure side near the trailing edge. When the entropy spot is convected close to these zones local sources of indirect noise appear.

The high pressure fluctuation areas shown in the Figure 19 act as noise sources within the stator channel generating acoustic spinning lobes at the EWF propagating in the upstream and downstream directions within the annular channel. The incoming entropy wave, characterized by 11 entropy spots synchronously released, can be thought as a superposition of spinning perturbations with the circumferential order $m_{ew} = 0, \pm 11, \pm 22, \pm 33, \pm h{\cdot}11, \ldots$ that generate the corresponding acoustic waves. Moreover, following the Tyler-Sofrin rule [36], each acoustic spinning perturbation is further scattered by the rotor blade with the formula $m_{aw} = m_{ew} \pm k{\cdot}22$. Due to the low frequency (116.6 Hz), only the $m_{aw} = 0$ is cut-on and propagates without decaying in the annular duct. For this reason, the overall acoustic power related to the indirect noise are carried by the $m_{aw} = 0$ azimuthal mode.

4.2.2. Rotor row

As shown in Figure 14, the EW spots enter the rotor with low intensity and are spread over the pitch above midspan. For this reason the indirect noise generation in the rotor channel, although possible due to the mean velocity gradient shown in Fig. 20, does not have a relevant impact on the overall emission at the stage inlet/outlet. To confirm this statement the zones with higher pressure fluctuations are plotted in Fig. 21 for the PS and SS clocking positions for which minimum and maximum temperature fluctuation entering the rotor are found respectively. Again, the blue transparent surfaces shows the borders of the entropy spot which is now spread over the entire

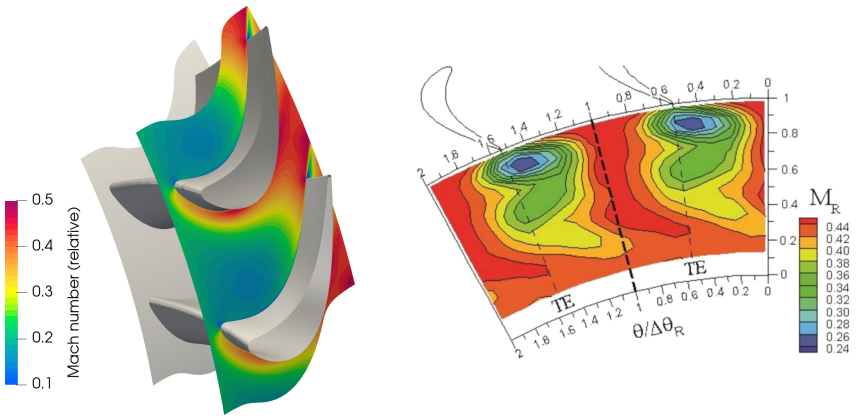

(a) (b)

Figure 20: Mach number field in the rotor field to highlight high gradient areas. (a) Blade-to-blade numerical contours, TRAF. (b) T2 plane experimental contours.

channel at different spanwise positions (as already shown in Fig. 15), while red solid surface highlight the zone where the pressure fluctuation is higher 116 dB (that is 4 dB lower than in the respective stator plot). The high pressure fluctuations areas within the rotor row are quite similar for the two clocking positions. The generation zones at the rotor leading edge are due to the downstream pressure wave (with $m_{aw} = 0$) generated within the stator that impinges on the rotor leading edge.

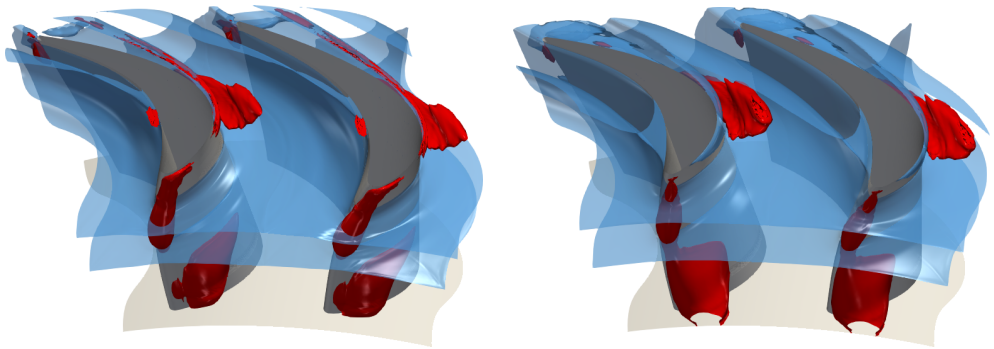

(a) (b)

Figure 21: Indirect noise generation areas in the rotor: (a) PS case, (b) SS case. Red solid surfaces delimit the zone where the pressure fluctuations are higher than 116 dB. Blue transparent contours depicts the entropy wave path (numerical results).

On the other hand, the small generation spot near the rotor throat at the blade tip can be identified as additional indirect noise generation regions for both clocking positions. For the SS case, this spot is slightly wider in agreement with the higher temperature fluctuation entering the rotor. Yet, when comparing the pressure fluctuation intensity of these indirect noise generation sources with the ones found in the stator channel, it is clear that their contribution to the overall emission can be considered negligible.

4.3. Indirect noise stage emission

The final outcomes of these numerical study are the evaluation and comparison (at the stage outlet for a single position) of the outgoing acoustic waves generated by the incoming EW in order to demonstrate the possibility of predicting the indirect noise emissions of high pressure turbine stage by using URANS simulations and a dedicated acoustic post-processing.

4.3.1. Stage inlet (plane T0)

The evaluation of the indirect noise emission at the stage inlet is based on the computation of the overall sound pressure lever PWL of the outgoing (upstream running, p_δ^-) acoustic waves. To do so, the time Fourier coefficients describing the pressure perturbation field are firstly circumferentially decomposed to extract the different circumferential patterns present in an annular duct. Then, from each spinning perturbation the upstream and downstream running components are separated to evaluate the acoustic intensity and finally their sound power (PWL). Figure 22 shows the circumferential decomposition of the pressure pressure field along the span at the T0 location for the SS case. The sign of the circumferential order defines the rotational direction of the spinning perturbation. As expected, the main perturbation is due to the standing wave ($m_{ac} = 0$), while the other spinning lobes are $m_{ac} = \pm 11, \pm 22, \ldots$ caused both from the entropy spot morphology and the stator scattering have a very low intensity.

According to the radial mode analysis concepts in annular ducts, each single acoustic perturbation is characterized by a radial shape that can be approximated with a Bessel function and by a radial order μ (the number of zero-crossing of the Bessel function). Looking at Fig. 22, it is clear that only the $\mu = 0$ (the only cut-on perturbations at this low frequency that is basically flat along the span) are present in the overall distribution for both up/downstream running waves at the $m_{ac} = 0$ azimuthal mode.

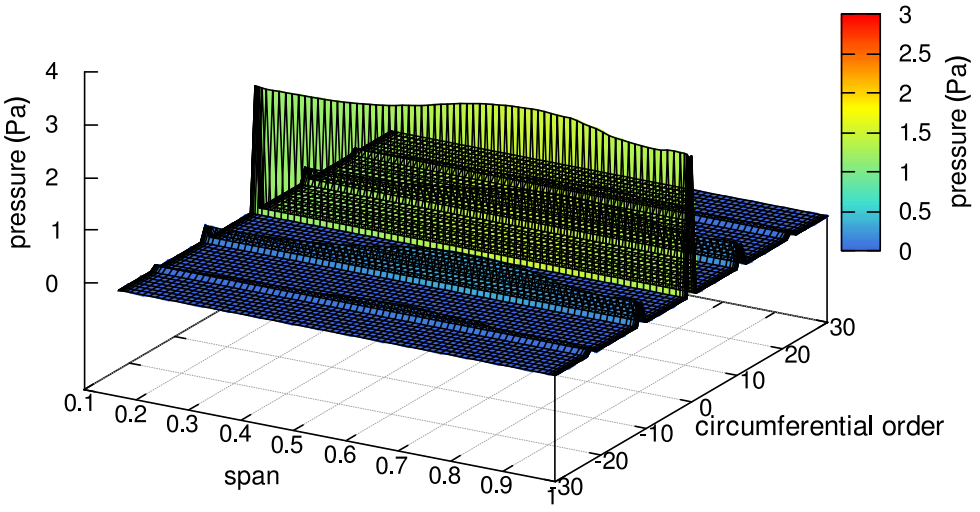

Figure 22: Circumferential decomposition of pressure perturbation at the stage inlet (plane T0) for the SS case.

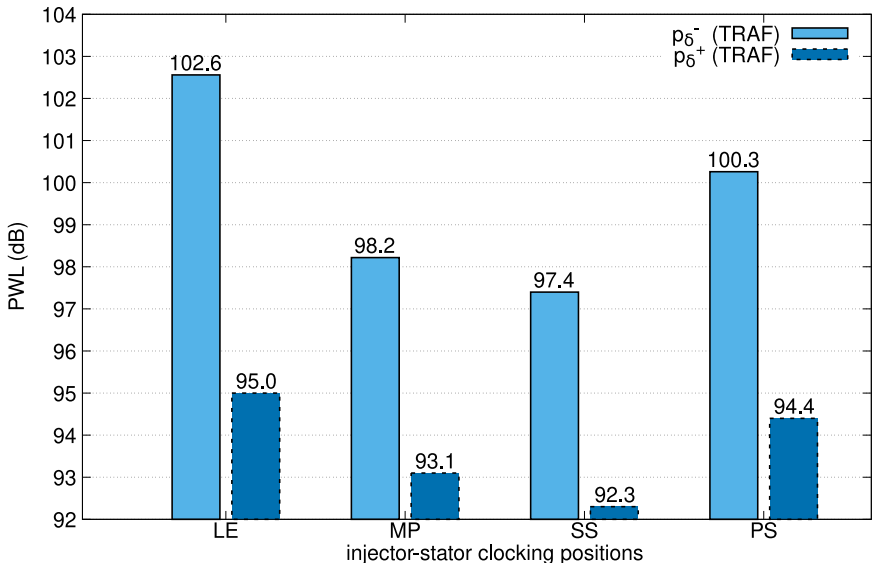

Figure 23: Sound power level at the stage inlet (plane T0): light blue bars represent the outgoing (upstream running) waves, dark blue dashed histograms report the downstream running waves (spurious reflections).

Finally, this azimuthal mode is further locally decomposed to extract upstream and downstream running pressure waves following the Giles theory [30] summarized in the post-processing section. Figure 23 reports the overall PWL at the stage inlet for both acoustic waves (p_δ^- and p_δ^+) for the different clocking positions. Looking at the upstream running waves, the following conclusions can be drawn:

- LE case shows the highest upstream running emission (102.5 dB) in agreement with what observed in Fig. 19(a), where the indirect noise generation areas are wider in the front part of the stator
- SS case has the lower outgoing emissions at the stage inlet, as the generation zones are the smallest as depicted in Fig. 19(c)
- PS and MP cases are in between as total emission, which have a second contribution from the noise generation spot placed on the pressure side near the trailing edge (see Fig. 19(d) and 19(b))

Figure 23 also reports the sound power level of the downstream running waves that are around 6 dB lower than the upstream ones thus confirming that the imposed EW does not add additional sound power and that the inlet boundary properly works as non reflective surface.

4.3.2. Stator outlet/rotor inlet (plane T1)

Although the noise experimental acquisition is not performed in this inter-row region, it is worth decomposing the acoustic pressure field in order to study the coupled acoustic field due to the reflection and transmission caused by upstream stator and downstream rotor rows. Indeed, downstream running pressure waves generated in the stator channel can be reflected back by the rotor row and interact with the upstream running components. Moreover, these upstream running reflections can be further reflected downstream by the stator generating a coupled pressure perturbation field in this region. Figure 24 reports the tangential decomposition of the pressure field along the span for SS case. The overall acoustic fluctuation at this section is higher than in the inlet region as the standing wave ($m_{ac} = 0$) has an average amplitude of about 10 Pa with maximum value near the hub. This azimuthal order is finally decomposed in upstream and downstream running waves which PWL values are reported in Figure 25.

Downstream running waves are around 2 dB higher than upstream ones for the different clocking positions confirming that the upstream running

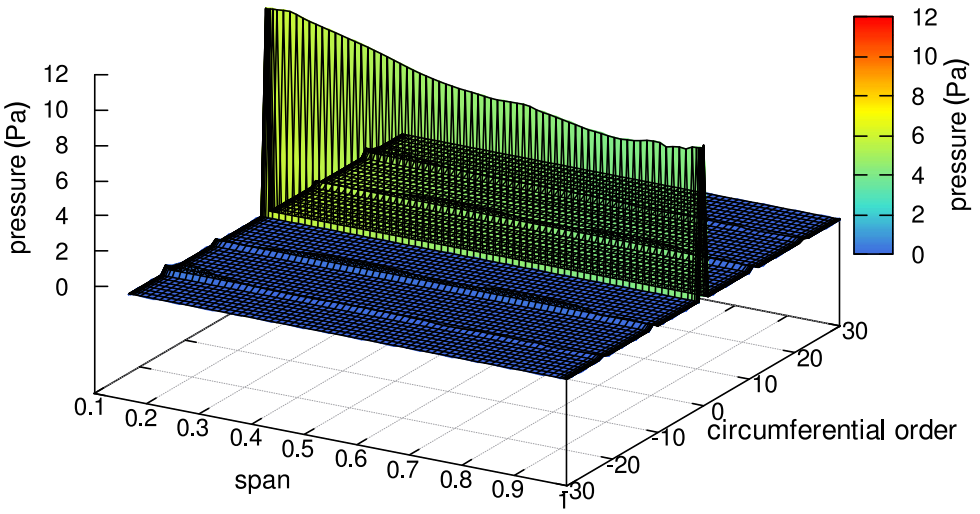

Figure 24: Circumferential decomposition of pressure perturbation at the inter-row section (plane T1) for the SS case.

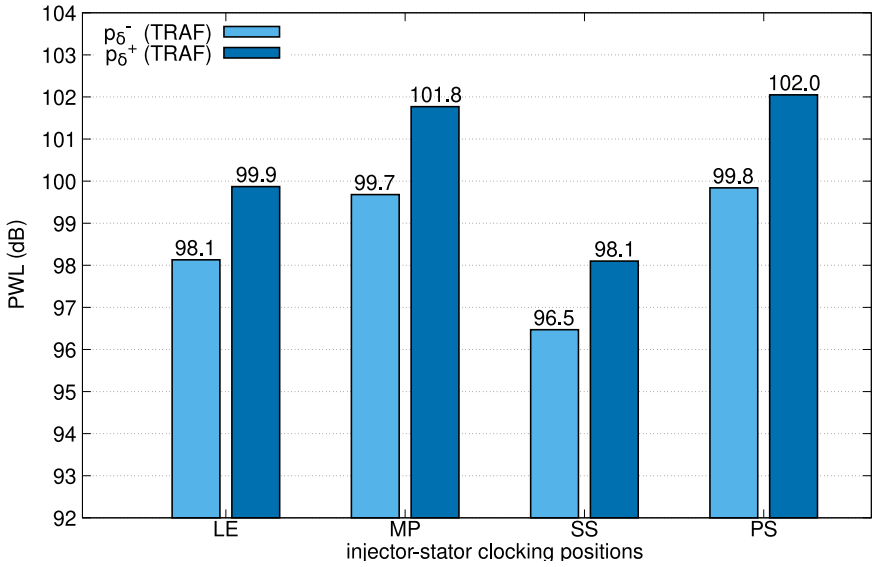

Figure 25: Sound power level at the inter-row section (plane T1): light blue bars represent the upstream running waves, dark blue histograms report the downstream running waves.

components are likely generated by the reflection of downstream waves with rotor rows. Focusing on the downstream running components which are basically due to indirect noise generation in the stator channel, it is evident that the highest emission occurs when noise generation zones are located near the stator trailing edge (case PS and MP, see Fig. 19). Case LE and SS have lower downstream running components as the indirect noise generation source are basically located near the leading edge (see again Fig. 19) and radiate mostly upstream.

Therefore, upstream running waves present at plane T1, contribute to the outgoing PWL at the stage inlet, while downstream running component are transmitted thorough the rotor row and are the principal contribution of the outgoing emissions at the stage outlet as shown in the following section.

4.3.3. Stage outlet (plane T2)

Finally, the acoustic wave decomposition is performed at the stage outlet to obtain the outgoing waves (downstream running, p_δ^+) and to compare the PWL value for the PS case with experimental acquisitions.

The azimuthal decomposition of the acoustic field for SS case in Figure 26 shows again the standing wave $m_{ac} = 0$ with a flat trend along the span direction which reveals the presence of a single radial mode cut-on with

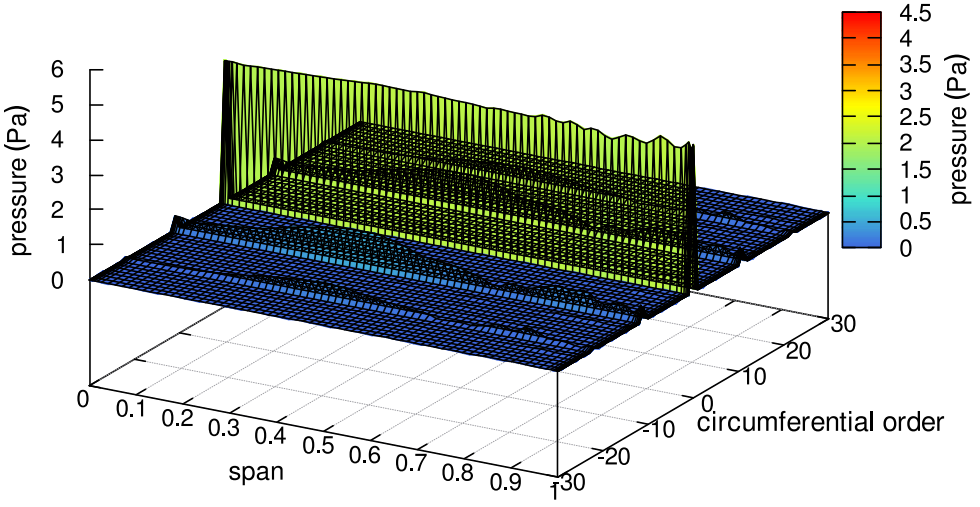

Figure 26: Circumferential decomposition of pressure perturbation at the stage outlet (plane T2) for the SS case.

$\mu = 0$. The analysis of PWL outgoing emissions at the stage outlet for the different injector positions (see Fig. 27) leads to the following comments.

- There is an excellent agreement between experimental and numerical values for the PS case. It is important to recall that an an anechoic termination is installed at the stage outlet within the test rig to avoid spurious reflections. Moreover, on the numerical side the use of the calibrated buffer zone mimics the experimental anechoic termination. Both aspects are essential for the accurate numerical and experimental comparison.

- The overall emission for the different clocking positions show similar levels (around 99/98 dB). Comparing these values with the inter-row one, it is clear that the outgoing wave are basically generated in the stator channel and undergo different transmission loss through the rotor.

- Small entropy noise generation zones are detected also in the rotor channel (see Fig. 21) near the blade throat. Yet such areas have a low

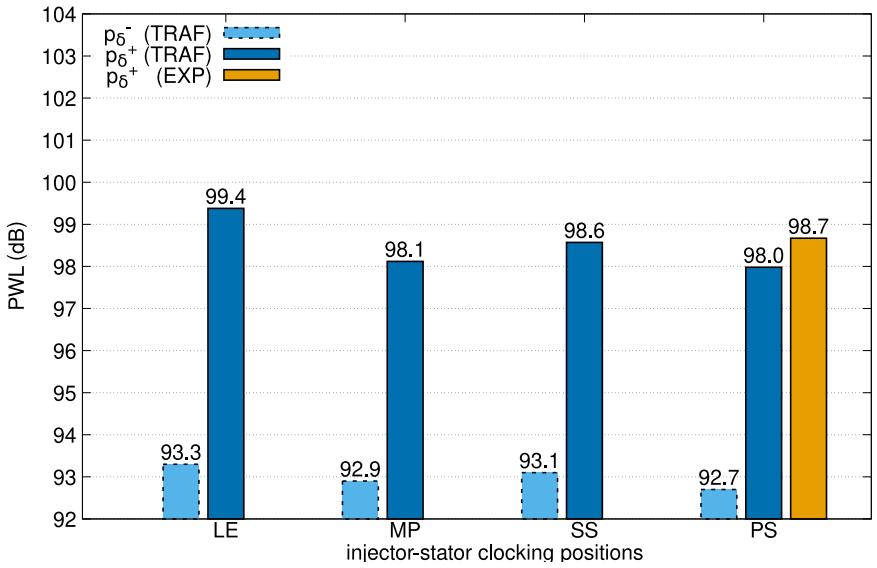

Figure 27: Sound power level at the stage outlet (plane T2): light blue dashed bars represent the upstream running waves (spurious reflections), dark blue histograms report the outgoing (downstream running) waves, yellow bar is the experimental value.

intensity respect to the ones found in the stator channel (4 dB lower) and have a negligible effect on the overall entropy noise emissions at the stage inlet/outlet.

- Upstream running waves p_δ^- are more than 6 dB lower respect to downstream ones thus confirming the correct working of the buffer zone treatment.

In conclusion, this activity has demonstrated the capability of URANS computations with a dedicated perturbation post-processing to correctly solve the evolution of entropy waves in a turbine stage and to accurately predict the indirect entropy noise emissions radiated from the stage. URANS method results a viable alternative to existing reduced-order models, like actuator disk theory, that may not able to capture the overall phenomenon, and to high-fidelity simulations that usually require a higher computational effort [15]. Such analyses and the post-processing outcomes can profitably be used by the designers to reduce the interaction between combustion chamber and high pressure turbine stage both in terms of thermal load and entropy noise generation.

5. Conclusions

The article describes the effect of clocking on entropy noise generation in an aeronautical high pressure turbine stage due to an engine-representative entropy wave entering the stage by means of detailed comparisons between experiments and simulations.

Experiments include unsteady aerodynamic and thermal measurements upstream and downstream of each blade row of the stage, and a microphone array between the stage outlet and an anechoic termination to acquire outgoing acoustic emissions.

The computational flow model makes use of state-of-the-art physical models, and a dedicated post-processing strategy based on time and space DFT to filter low-frequency content fluctuation from the unsteady solution of the stage with a pulsating inlet. The unsteady post-processing has been also extended to identify the stage zones where indirect noise generation occurs and finally to separate upstream and downstream running acoustic waves composing the entropy noise emissions.

The presented results reveal that the main sources of entropy noise are located in the stator channel and depend on the clocking position of the temperature spots. The indirect noise generation areas are located at the stator leading edge on the suction side for all the clocking positions and also on the pressure side near the trailing edge for midpitch (MP) and pressure side (PS) cases, explaining the different acoustic emissions at the stage inlet and outlet. Acoustic post-processing in the inter-row region confirms the presence of a coupled pressure field caused by the downstream emission generated within the stator and reflected back by the rotor. Finally a small area of indirect noise generation was found in the rotor channel near the throat, but (due to its low intensity) this additional noise source has a negligible effect on the overall emission at the entropy wave frequency.

All the experimental and numerical comparisons on the entropy wave evolution and indirect noise emission reported in the paper validate the proposed numerical approach and demonstrate the possibility to use URANS simulations to predict entropy noise generation in a HP turbine stage.

Such simulations, although computational demanding, can be applied for parametric studies concerning the clocking position of the perturbation source to reduce the turbine conbustor interactions and the indirect noise emission. Moreover, numerical results can also exploited for a detailed analysis of the dominating noise generating locations within the turbine stage.

References

[1] W. Neise, L. Enghardt, Technology approach to aero engine noise reduction, Aerosp. Sci. Technol. 7 (5) (2003) 352–363. doi:https://doi.org/10.1016/S1270-9638(03)00027-0.

[2] A. S. Morgans, I. Durán, Entropy noise: A review of theory, progress and challenges, Int. J. Spray Combust. Dyn. 8 (2016) 285 – 298. doi:https://doi.org/10.1177%2F1756827716651791.

[3] D. Yang, J. Guzmán-Iñigo, A. S. Morgans, Sound generation by entropy perturbations passing through a sudden flow expansion, J. Fluid Mech. 905 (2020) R2. doi:10.1017/jfm.2020.849.

[4] C. Morfey, Amplification of aerodynamic noise by convected flow inhomogeneities, J. Sound Vib. 31 (4) (1973) 391–397. doi:https://doi.org/10.1016/S0022-460X(73)80255-X.

[5] F. Marble, S. Candel, Acoustic disturbance from gas non-uniformities convected through a nozzle, J. Sound Vib. 55 (2) (1977) 225–243. doi:https://doi.org/10.1016/0022-460X(77)90596-X.

[6] N. Cumpsty, F. Marble, The interaction of entropy fluctuations with turbine blade rows; a mechanism of turbojet engine noise, Proc. R. Soc. Lond. A Math. Phys. Sci., 1977, a357323–344. doi:http://doi.org/10.1098/rspa.1977.0171.

[7] S. Moreau, I. Duran, Analytical and numerical study of the entropy wave generator experiment on indirect combustion noise, in: 17th AIAA/CEAS Aeroacoustics Conference (32nd AIAA Aeroacoustics Conference). doi:10.2514/6.2011-2829.

[8] F. Bake, N. Kings, A. Fischer, I. Röhle, Experimental investigation of the entropy noise mechanism in aero-engines, Int. J. Aeroacoustics. 8 (1) (2009) 125–141. doi:10.1260/147547209786234966.

[9] S. K. Lele, J. W. Nichols, A second golden age of aeroacoustics?, Philosophical Transactions of the Royal Society A: Mathematical, Physical and Engineering Sciences 372 (2022) (2014) 20130321. doi:10.1098/rsta.2013.0321.

[10] F. Bake, N. Kings, I. Roehle, Fundamental Mechanism of Entropy Noise in Aero-Engines: Experimental Investigation, J. Eng. Gas Turbines Power 130 (1), 011202 (01 2008). doi:10.1115/1.2749286.

[11] M. Huet, A. Emmanuelli, T. Le Garrec, Entropy noise modelling in 2d choked nozzle flows, J. Sound Vib. 488 (2020) 115637. doi:https://doi.org/10.1016/j.jsv.2020.115637.

[12] I. Duran, S. Moreau, Solution of the quasi-one-dimensional linearized euler equations using flow invariants and the magnus expansion, J. Fluid Mech. 723 (2013) 190–231. doi:10.1017/jfm.2013.118.

[13] K. Knobloch, L. Neuhaus, F. Bake, P. Gaetani, G.Persico, Experimental assessment of noise generation and transmission in a high-pressure transonic turbine stage, ASME J. Turbomach. 139, 101006 (2017).

[14] K. Hu, Y. Fang, Y. Zheng, G. Wang, S. Moreau, Numerical investigation of influence of entropy wave on the acoustic and wall heat transfer characteristics of a high-pressure turbine guide vane, Acoust. 2 (3) (2020) 524–538. doi:10.3390/acoustics2030028.

[15] J. Winkler, J. M. Mendoza, Lattice boltzmann simulations of wave propagation through a high-pressure turbine stage, in: AIAA AVIATION 2021 FORUM, 2021, August 2-6, virtual event. doi:10.2514/6.2021-2260.

[16] C. Becerril, S. Moreau, L. Y. M. Gicquel, Study of Combustion Noise Generation in a Realistic Turbine Stage Configuration, Vol. Volume 2B: Turbomachinery of Turbo Expo: Power for Land, Sea, and Air, 2018. doi:10.1115/GT2018-75062.

[17] P. Gaetani, G. Persico, A. Spinelli, Coupled effect of expansion ratio and blade loading on the aerodynamics of a high-pressure gas turbine, Appl. Sci. 7, 259 (2017).

[18] G. Persico, P. Gaetani, A. Spinelli, Assessment of synthetic entropy waves for indirect combustion noise experiments in gas turbines, Exp. Therm. Fluid Sci. 88 (2017) 376–388.

[19] P. Gaetani, G. Persico, L. Pinelli, M. Marconcini, R. Pacciani, Computational and Experimental Study of Hot Streak Transport Within the First Stage of a Gas Turbine, ASME J. Turbomach. 142 (8), 081002 (07 2020). doi:10.1115/1.4045961.

[20] L. Pinelli, M. Marconcini, R. Pacciani, P. Gaetani, G. Persico, Computational and Experimental Study of the Unsteady Convection of Entropy Waves Within a High-Pressure Turbine Stage, ASME J. Turbomach. 143 (9), 091011 (05 2021). doi:10.1115/1.4050600.

[21] P. Gaetani, G. Persico, Technology development of fast-response aerodynamic pressure probes, Int. J. Turbomach. Propuls. Power 5 (2) (2020). doi:10.3390/ijtpp5020006.

[22] A. Arnone, Viscous analysis of three-dimensional rotor flow using a multigrid method, ASME J. of Turbomach. 116 (1994) 435–445.

[23] R. Pacciani, M. Marconcini, A. Arnone, Comparison of the AUSM+-up and other advection schemes for turbomachinery applications, Shock Waves 29 (01 2019). doi:10.1007/s00193-018-0883-4.

[24] D. C. Wilcox, Turbulence Modeling for CFD, 2nd Edition, DCW Ind. Inc., La Cañada, CA, USA, 1998, iSBN 1-928729-10-X.

[25] A. Arnone, M. S. Liou, L. A. Povinelli, Integration of Navier–Stokes Equations Using Dual Time Stepping and a Multigrid Method, AIAA J. 33 (6) (1995) 985–990.

[26] M. Giovannini, M. Marconcini, A. Arnone, A. Dominguez, A Hybrid Parallelization Strategy of a CFD Code for Turbomachinery Applications, in: 11^{th} European Conference on Turbomachinery Fluid Dynamics and Thermodynamics, 2015, madrid, Spain, 23–27 March 2015.

[27] M. Marconcini, A. Bianchini, M. Checcucci, G. Ferrara, A. Arnone, L. Ferrari, D. Biliotti, D. T. Rubino, A Three-Dimensional Time-Accurate Computational Fluid Dynamics Simulation of the Flow Field Inside a Vaneless Diffuser During Rotating Stall Conditions, ASME J. Turbomach. 139 (2) (2017) 021001.

[28] L. Pinelli, F. Lori, M. Marconcini, R. Pacciani, A. Arnone, Validation of a modal work approach for forced response analysis of bladed disks, Appl. Sci. 11 (12) (2021). doi:10.3390/app11125437.

[29] L. Pinelli, F. Poli, E. Di Grazia, A. Arnone, D. Torzo, A comprehensive numerical study of tone noise emissions in a multistage cold flow rig, in: 19^{th} AIAA/CEAS Aeroacoustic Conference, 2013, AIAA paper 2013-2104, 27-29 May, Berlin, Germany.

[30] M. B. Giles, Nonreflecting boundary conditions for euler equation calculations, AIAA J. 28 (12) (1990) 2050–2058. doi:10.2514/3.10521.

[31] M. Marconcini, F. Rubechini, A. Arnone, A. Scotti Del Greco, R. Biagi, Aerodynamic Investigation of a High Pressure Ratio Turbo-Expander for Organic Rankine Cycle Applications, Vol. Volume 8: Turbomachinery, Parts A, B, and C of Turbo Expo: Power for Land, Sea, and Air, 2012, pp. 847–856. doi:10.1115/GT2012-69409.

[32] M. K. Myers, Transport of energy by disturbances in arbitrary steady flow, J. Fluid Mech. 226 (1991) 383–400.

[33] L. Pinelli, L. Lilli, A. Arnone, P. Gaetani, G. Persico, Numerical study of entropy wave evolution within a hpt stage, E3S Web Conf. 197 (2020) 11011. doi:10.1051/e3sconf/202019711011.

[34] D. J. Bodony, Scattering of an entropy disturbance into sound by a symmetric thin body, Phys. Fluids 21 (9) (2009) 096101. doi:10.1063/1.3225143.

[35] J. Guzmán-Iñigo, I. Durán, A. Morgans, Scattering of entropy waves into sound by isolated aerofoils, J. Fluid Mech. 923 (2021) A10. doi:10.1017/jfm.2021.569.

[36] J. Tyler, T. Sofrin, Axial flow compressor noise studies, Trans. Society of Automotive Engineers 70 (1962) 309–332.